

Stripped gas as fuel for newly formed HII regions in the encounter between VCC1249 and M49: a unified picture from NGVS and GUViCS.

Fabrizio Arrigoni Battaia^{1,2}, Giuseppe Gavazzi², Michele Fumagalli³, Alessandro Boselli⁴, Samuel Boissier⁴, Luca Cortese⁵, Sebastien Heinis⁴, Laura Ferrarese⁶, Patrick Côté⁶, J. Christopher Mihos¹⁰, Jean Charles Cuillandre⁷, Pierre-Alain Duc¹², Patrick Durrell¹¹, Stephen Gwyn⁶, Andrés Jordán⁹, Chengze Liu¹³, Eric Peng⁸, Simona Mei^{14,15,16}

¹ Max-Planck-Institut für Astronomie, Königstuhl 17, D-69117 Heidelberg, Germany
e-mail: arrigoni@mpia.de

² Dipartimento di Fisica G. Occhialini, Università di Milano- Bicocca, Piazza della Scienza 3, 20126 Milano, Italy
e-mail: giuseppe.gavazzi@mib.infn.it

³ Department of Astronomy and Astrophysics, University of California, 1156 High Street, Santa Cruz, CA 95064, USA
e-mail: mfumagalli@ucolick.org

⁴ Laboratoire d'Astrophysique de Marseille - LAM, Université d'Aix-Marseille & CNRS, UMR7326, 38 rue F. Joliot-Curie, 13388 Marseille Cedex 13, France
e-mail: alessandro.boselli@oamp.fr; samuel.boissier@oamp.fr; Sebastien.heinis@oamp.fr

⁵ European Southern Observatory, Karl-Schwarzschild Strasse 2, 85748 Garching bei Muenchen, Germany
e-mail: lcortese@eso.org

⁶ Herzberg Institute of Astrophysics, National Research Council of Canada, Victoria, BC V9E 2E7, Canada
e-mail: Laura.Ferrarese@nrc-cnrc.gc.ca; patrick.cote@nrc-cnrc.gc.ca; Stephen.Gwyn@nrc-cnrc.gc.ca

⁷ CFHT corporation, 65-1238 Mamalahoa Highway, Kamuela, Hawaii 96743, USA
e-mail: jcc@cfht.hawaii.edu

⁸ Kavli Institute for Astronomy and Astrophysics, Peking University, Beijing 100871, China
e-mail: peng@pku.edu.cn

⁹ Departamento de Astronomía y Astrofísica, Pontificia Universidad Católica de Chile, Vicuna Mackenna 4860, 7820436 Macul, Santiago, Chile
e-mail: ajordan@astro.puc.cl

¹⁰ Department of Astronomy, Case Western Reserve University, 10900 Euclid Ave, Cleveland, OH 44106, USA
e-mail: mihos@case.edu

¹¹ Department of Physics & Astronomy, Youngstown State University, Youngstown, OH 44555, USA
e-mail: prdurrell@ysu.edu

¹² Laboratoire AIM, CEA/DSM-CNRS-Université Paris Diderot, Dapnia/Service d'Astrophysique, CEA-Saclay, 91191 Gif-sur-Yvette Cedex, France
e-mail: paduc@cea.fr

¹³ INPAC and Department of Physics, Shanghai Jiao Tong University, 800 Dongchuan Road, Shanghai 200240, China
e-mail: czliu@pku.edu.cn

¹⁴ GEPI, Observatoire de Paris, Section de Meudon, 5 Place J. Janssen, 92190 Meudon Cedex, France
e-mail: simona.mei@obspm.fr

¹⁵ Université Paris Denis Diderot, 75205 Paris Cedex 13, France

¹⁶ California Institute of Technology, Pasadena, CA 91125, USA

Received 26/01/2012; accepted 30/04/2012

ABSTRACT

Context. We study the peculiar interacting galaxy system of VCC1249/M49 located in the core of the Virgo B subcluster. Owing to a recent interaction between the dwarf galaxy VCC1249 and the halo gas of the elliptical galaxy M49, neutral hydrogen has been displaced from the interstellar medium of this dwarf into the Virgo intracluster medium. Observations also reveal multiple compact star-forming regions (*aka* HII regions) that are embedded in this HI cloud, with a projected separation up to 13 kpc from VCC1249 in the northwest direction.

Aims. Motivated by recent near-ultraviolet (NUV) imaging from the GALEX Ultraviolet Virgo Cluster Survey (GUViCS) of the VCC1249/M49 system that shows significant ongoing/recent star formation in the compact regions, we aim to constrain the origin of these outlying HII regions with a multi-wavelength approach.

Methods. Using deep optical (u, g, i, z) imaging from the Next Generation Virgo Cluster Survey (NGVS) and new H α imaging obtained at the San Pedro Martir observatory together with Keck long-slit spectroscopy, we characterize the star formation rates, ages, and metallicity of VCC1249 and its outlying compact regions. Moreover, we analyze the color and luminosity profile of the galaxy to investigate its recent interaction with M49.

Results. Our new observations indicate that VCC1249 underwent a recent interaction with M49 in which both ram-pressure stripping and tidal interaction occurred. The joint action of the two mechanisms led to the removal of the HI gas from the interstellar medium of VCC1249, while the gravitational tides triggered the stellar tail and counter-tail of VCC1249. Our stellar population synthesis analysis reveals that the star formation in this galaxy was truncated around 200 Myr ago and that the outlying HII regions were born *in situ* \approx 10 Myr ago out of pre-enriched gas removed from the dwarf galaxy. These observations also reveal that interactions between central and satellite galaxies similar to those between VCC1249/M49 may be an effective way of dispersing metals into the halos of massive galaxies.

Key words. Galaxies: clusters: individual: Virgo; Galaxies evolution; Galaxies irregular

1. Introduction

The role of the environment in shaping the observed properties of galaxies (morphology, star formation, color, gas content, etc.) during their evolution is the subject of an ongoing debate. Among the multiple processes that operate in dense environments (see the review by Boselli & Gavazzi 2006), ram-pressure stripping (Gunn & Gott 1972) is often invoked as the principal mechanism acting in clusters, especially on dwarf galaxies. Indeed, due to their shallower gravitational potential, the dynamical pressure that originates from the fast motion of these galaxies through the hot and dense intra-cluster medium (ICM) can easily exceed the gravitational binding force in the galaxy and efficiently remove atomic gas from their interstellar medium (ISM). The resulting sudden suppression of the star formation in these stripped galaxies, then, leads to their temporary transformation into post star-burst (K+A; Poggianti et al. 2004), and subsequently into dE galaxies (Gavazzi et al. 2010). Ram-pressure stripping can therefore be the leading mechanism for the migration of dwarf galaxies from the blue cloud to the red sequence (Boselli et al. 2008a,b).

Stripped neutral hydrogen is frequently observed in the local Universe. For instance, extended HI tails are observed in the Virgo cluster (Chung et al. 2007, 2009) associated with late-type galaxies within 1 Mpc projected distance from M87. Because the stripped gas always points away from the cluster center, these tails are a clear signature of the ram-pressure mechanism. Another typical feature of a ram-pressure stripped tail is the absence of a stellar counterpart. Moreover, galaxies that are infalling in rich clusters occasionally show stripped gas with associated star formation (Cortese et al. 2007), as evident from their ultraviolet (UV) (Smith et al. 2011), H α (Yagi et al. 2010), and X-ray emission (Sun et al. 2010). A remarkable example is the dwarf irregular (dIrr) galaxy VCC1217, which shows an extended tail of bright knots and of diffuse emission in the UV light (Hester et al. 2010; Fumagalli et al. 2011), which is associated to star formation triggered by the interaction with the intergalactic medium. This interpretation is also consistent with the findings of hydrodynamic simulations (Kapferer et al. 2009).

In addition to hydrodynamic processes, tidal interactions (e.g. Spitzer & Baade 1951; Valluri & Jog 1990; Duc & Renaud 2011) can efficiently remove baryons from galaxies, in particular from the outer and less bound regions. However, because of the high relative velocities among cluster galaxies, these encounters occur on shorter time scales than in the field, resulting in a less severe disturbance of the galaxy stellar and gaseous disks. Moreover, galaxies in clusters grow through merging and accretion processes, consistent with hierarchical models and as indicated by the extensive web of low-surface brightness filaments and tidal features found by Janowiecki et al. (2010) in the intracluster light around luminous ellipticals in Virgo (M49, M87, M86, M89). Perhaps the most spectacular example of an interacting system in the Virgo cluster is that between NGC4438 and M86, whose morphology and gas content require that tidal interaction and ram-pressure stripping are simultaneously occurring (Kenney et al. 2008). Similarly, the perturbations observed in NGC4654 and NGC4254 can be modeled with a close encounter with a nearby companion combined with ram-pressure stripping (Vollmer 2003; Vollmer et al. 2005).

Environmental processes may also play a role in the formation of ultra compact dwarfs (UCD; Drinkwater et al. 2000), a new class of objects in clusters whose stellar masses exceed those observed in the brightest globular clusters only by small amounts (Haşegan et al. 2005; Mieske et al. 2008). However,

their origin is controversial. One hypothesis is that they derive from stripping of dE galaxies in the cluster potential or the potential of its brightest members (“threshing scenario” Bekki et al. 2003). Alternatively, a merger of young and massive star clusters that formed during an interaction between gas-rich galaxies (Kroupa 1998; Fellhauer & Kroupa 2002) could account for the origin of UCDs.

Similar arguments apply to the rare class of compact elliptical (cE) galaxies, such as M32, whose compact nature has been ascribed to tidal stripping (e.g., Faber 1973; Bekki et al. 2001; Huxor et al. 2011).

In this paper, we focus on the interaction between the dIrr galaxy VCC1249 (*aka* UGC 7636) and the massive elliptical M49. The system VCC1249/M49 has been studied previously, following the detection of an HI cloud displaced from the galaxy in the direction of M49 (Sancisi et al. 1987; Patterson & Thuan 1992; Henning et al. 1993). Subsequently, McNamara et al. (1994) found a trail of debris that does not coincide with the HI gas and is projected northward from the dwarf galaxy¹. Lee et al. (1997, 2000) furthermore showed the presence of young HII regions embedded in the HI cloud. The conclusions of these studies is that both ram-pressure stripping and tidal interaction are necessary to explain the morphology and the deficiency of HI in VCC1249.

Our attention was again caught by the VCC1249/M49 system owing to a recent deep NUV GALEX image, obtained as part of the GALEX Ultraviolet Virgo Cluster Survey (GUViCS) (Boselli et al. 2011), showing an extended UV feature stretching from VCC1249 toward M49, with some relative maxima in correspondence with the detached HI emission. By combining these new data to high-quality optical imaging data from the Next Generation Virgo Cluster Survey (NGVS) (Ferrarese et al. 2011) at CFHT and with Keck optical spectroscopy of the external HII regions embedded in the HI cloud, we are able to conduct the first multiwavelength analysis of the properties of VCC1249 and of the outlying HII regions. In particular, following a procedure similar to Fumagalli et al. (2011) for VCC1217, we adopt a spectral energy distribution (SED) fitting technique to constrain the age of external HII regions and the epoch at which the star formation in VCC1249 was suddenly truncated, presumably by the interaction with M49. We stress that the ram-pressure mechanism we are referring to throughout this work is not caused by the ICM within the Virgo Cluster, but by the hot and dense halo of M49, as described in Mayer et al. (2006).

The organization of the present paper is as follows: in § 2, we discuss the observations and data reduction for each band. The properties of VCC1249 and of the external star-forming regions are studied in § 3 and § 4, respectively. In § 5 we show the results of the SED fitting analysis for both VCC1249 and the HII regions and in § 6 we summarize our conclusions and present a panoramic view of the Virgo’s B subcluster updated accordingly.

Throughout this paper we assume a standard cosmology and a distance modulus of 31.14 ± 0.05 mag for M49 corresponding to the distance of 16.9 ± 0.3 Mpc (Mei et al. 2007), fully consistent with 16.7 ± 0.5 Mpc from Blakeslee et al. (2009) and with 17.0 Mpc from Gavazzi et al. (1999). Magnitudes are given in the AB system throughout the paper.

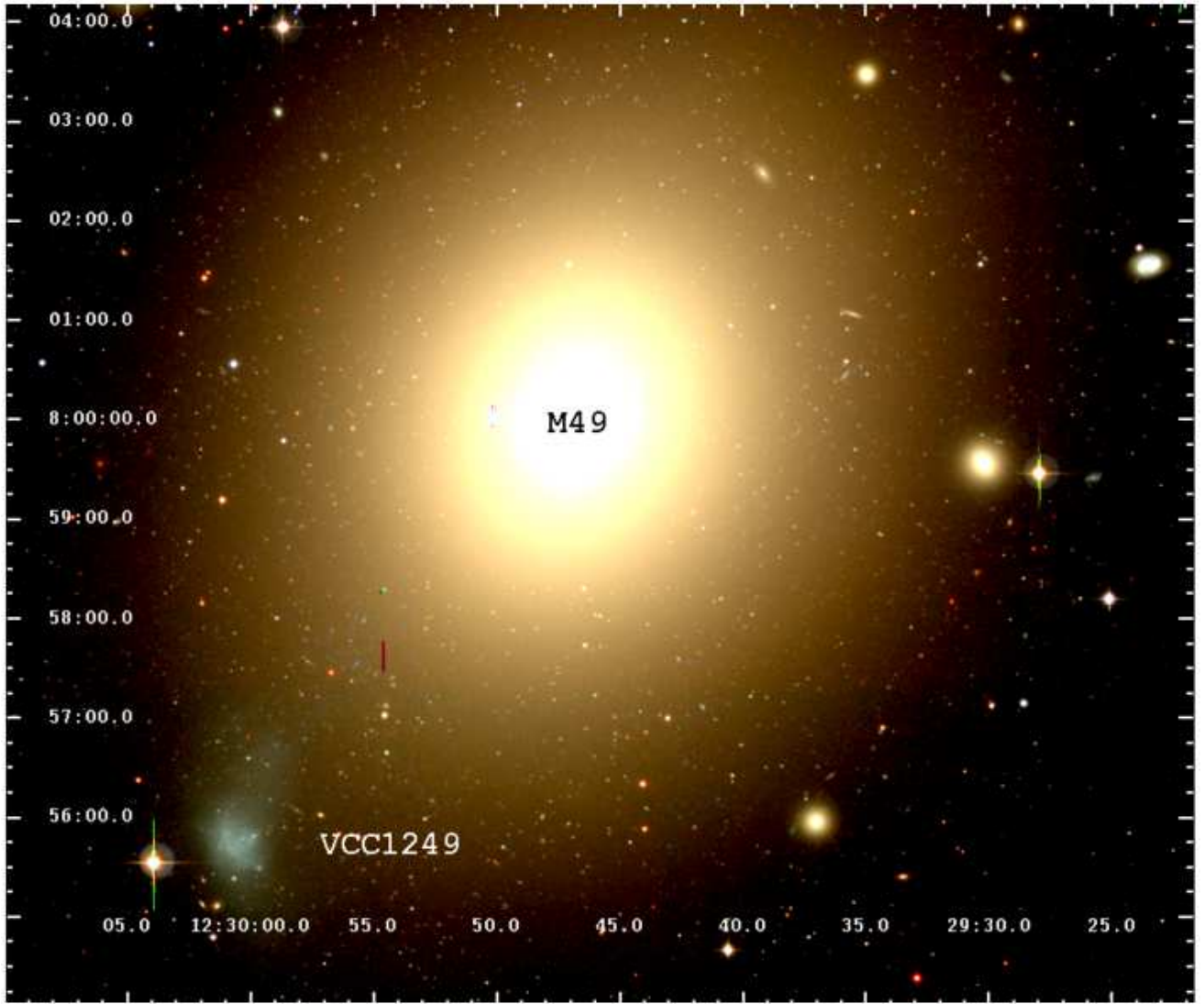


Fig. 1. RGB image of VCC1249 (bottom-left) and of M49 (center) obtained by combining the NGVS images in the u, g, z filters. The difference in color between the red giant elliptical M49 and the blue dIrr VCC1249 is apparent. The faint tidal tail of VCC1249 is also visible in the northwest direction.

Table 1. Log of the observations.

Imaging				
Telescope	Filter	Seeing (arcsec)	Date (yyyy-mm-dd)	Exp. Time (sec)
CFHT	u -NGVS	0.96	2009-02-27	6402
CFHT	g -NGVS	0.71	2009-02-22	3170
CFHT	i -NGVS	0.61	2009-02-18	2050
CFHT	z -NGVS	0.82	2009-02-22	4400
GALEX	NUV	5.3	2010-03-19	1631
GALEX	FUV	4.2	2004-04-17	104
SPM	$H\alpha$ 6603	1.5	2011-04-25	3×600
SPM	r'	1.5	2011-04-25	300
Spectroscopy				
Telescope	Instrument	Slit/Fiber (arcsec)	Date (yyyy-mm-dd)	Exp. Time (sec)
Keck	LRIS	1.0	2011-01-3	2×1200
Keck	LRIS	1.0	2011-01-4	900
Lick	KAST	2.0	2011-04-29	2×1800
SDSS	SDSS	3.0	DR7	2040

2. Observations and data reduction

Since 2009 we have collected new deep observations of the system VCC1249/M49, covering a wide stretch of the electromagnetic spectrum, including UV (NUV), optical imaging ($u, g, i, z + H\alpha$), and optical spectroscopy. A summary of these observations is presented in Table 1. In this section, we present a brief description of these observations and of the data reduction.

¹ This feature and the similarity in shape of the HI cloud and galaxy (see Figure 6) are the two strongest signatures for the ram-pressure mechanism highlighted by McNamara et al. (1994).

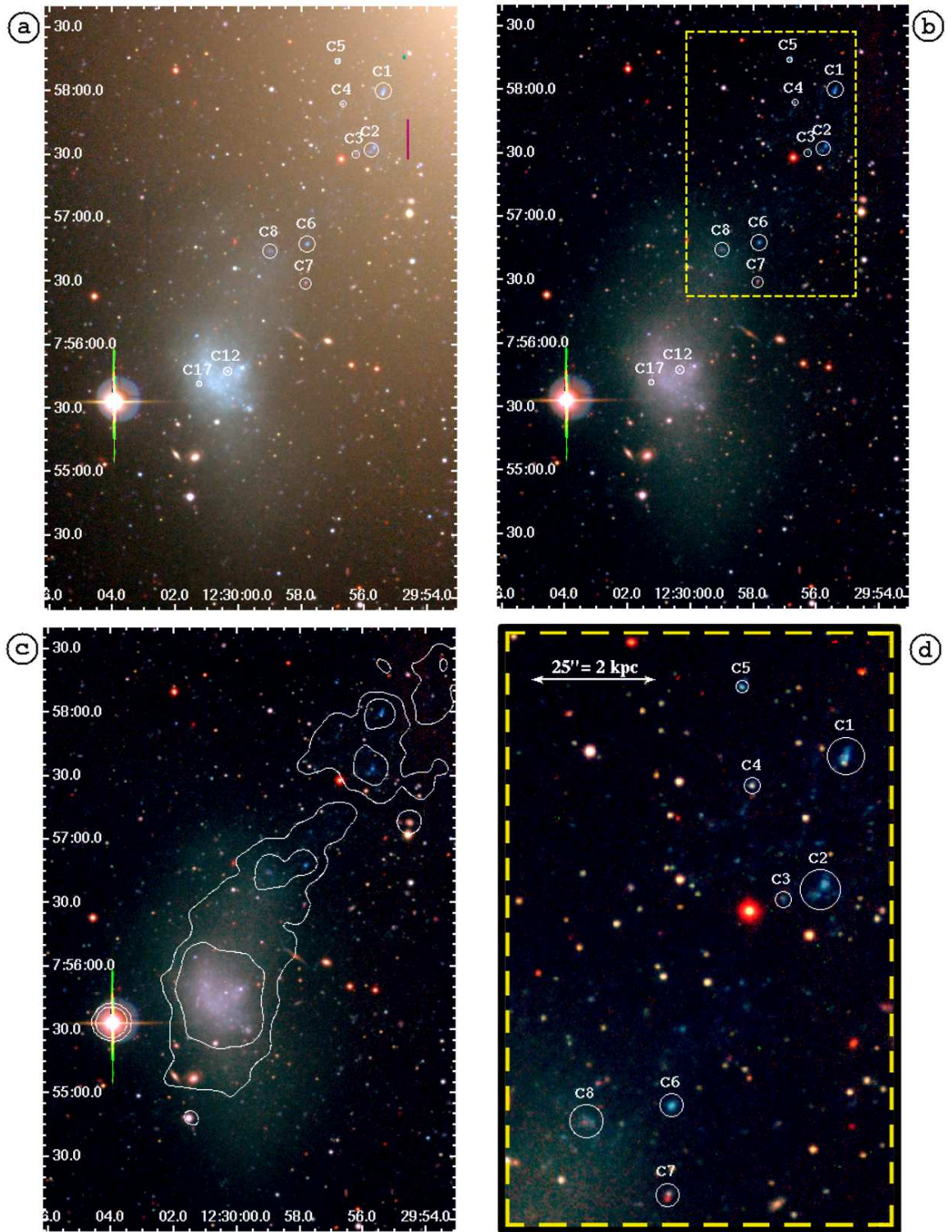


Fig. 2. (a) RGB image of VCC1249 obtained combining the NGVS images in the u, g, z filters. The outlying HII regions studied in this work are highlighted. Contamination from the light associated with the halo of M49 is clearly visible. (b) RGB image of VCC1249 obtained after subtracting a model for the light distribution in M49. (c) NUV contours superposed on the RGB image of VCC1249, after subtracting M49. (d) Enlargement of the region enclosed in the dashed yellow box in panel (b). Faint blue structures are visible near the highlighted HII regions.

Images and spectra were analyzed using the STSDAS and GALPHOT² routines in the IRAF³ and FUNTOOLS⁴ packages.

² Developed for IRAF - STSDAS mainly by W. Freudling, J. Salzer, and M.P. Haynes (see Haynes et al. 1999) and adapted by L. Cortese and S. Zibetti to handle H α data.

³ IRAF is the Image Analysis and Reduction Facility made available to the astronomical community by the National Optical Astronomy Observatories, which are operated by AURA, Inc., under contract with the U.S. National Science Foundation. STSDAS is distributed by the

Table 2. Aperture photometry corrected for extinction in the Milky Way of the two galaxies and of the star-forming regions. The photometry of M49 is computed within an aperture of about 5.7 arcmin radius (or $\sim 1.6 R_e$; Ferrarese et al. 2006).

ID	Distance (arcsec)	u (mag)	g (mag)	i (mag)	z (mag)	NUV (mag)	FUV (mag)
(1)	(2)	(3)	(4)	(5)	(6)	(7)	(8)
VCC1249	0	15.60 ± 0.03	14.73 ± 0.03	14.19 ± 0.03	14.11 ± 0.03	17.46 ± 0.15	18.68 ± 0.18
M49	334.0	10.28 ± 0.03	8.83 ± 0.03	7.81 ± 0.03	7.49 ± 0.03	13.91 ± 0.15	14.82 ± 0.17
C1	151.4	21.33 ± 0.04	21.31 ± 0.04	21.53 ± 0.04	22.12 ± 0.04	20.77 ± 0.16	20.80 ± 0.29
C2	126.1	21.31 ± 0.04	21.41 ± 0.04	21.83 ± 0.04	22.51 ± 0.05	21.52 ± 0.16	21.09 ± 0.32
C3	119.4	23.53 ± 0.06	23.27 ± 0.06	23.15 ± 0.05	23.00 ± 0.06	-	-
C4	137.9	23.09 ± 0.05	22.56 ± 0.06	22.33 ± 0.04	22.28 ± 0.04	(23.04 ± 0.15)	(22.48 ± 0.40)
C5	156.4	22.91 ± 0.05	22.69 ± 0.05	23.00 ± 0.05	23.28 ± 0.05	-	-
C6	70.7	21.92 ± 0.04	21.94 ± 0.04	22.31 ± 0.04	22.10 ± 0.04	21.37 ± 0.16	21.17 ± 0.33
C7	55.1	23.17 ± 0.06	22.87 ± 0.06	21.75 ± 0.04	21.22 ± 0.03	-	-
C8	61.1	22.31 ± 0.06	22.15 ± 0.06	22.14 ± 0.05	21.69 ± 0.04	21.43 ± 0.16	20.98 ± 0.31
C12	5.8	22.17 ± 0.06	21.48 ± 0.07	21.11 ± 0.06	21.10 ± 0.05	-	-
C17	19.2	23.94 ± 0.09	22.81 ± 0.16	22.03 ± 0.06	22.08 ± 0.06	-	-

(1) Naming of the star-forming regions as in Lee et al. (1997), (2) projected distance from the center of VCC1249. The photometric uncertainties are the quadratic sum of the ZP error and the Poisson error.

The whole photometry was corrected for Galactic extinction assuming $E(B - V) = 0.022$ from Schlegel, Finkbeiner & Davis (1998) and the Milky Way extinction law such that $A_{FUV} = 8.38E(B - V)$, $A_{NUV} = 8.74E(B - V)$, $A_u = 4.90E(B - V)$, $A_g = 3.70E(B - V)$, $A_i = 2.00E(B - V)$ and $A_z = 1.45E(B - V)$. Similarly, a 6 % correction was applied to $H\alpha$ for extinction in the Milky Way.

2.1. Optical imaging: NGVS

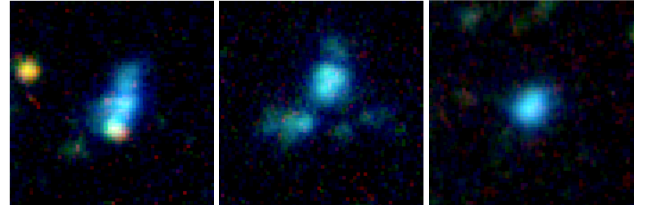
The system VCC1249/M49 was observed in the optical bands (u, g, i, z) as part of the NGVS⁵ under excellent seeing conditions (≤ 1 arcsec, see Table 1). The exposure times for each filter are listed in Table 1. Images were reduced and calibrated using a dedicated data reduction pipeline (Ferrarese et al. 2011) designed explicitly to recover faint, diffuse surface brightness features, reaching a surface brightness limit of $\mu_g = 29$ mag arcsec⁻² (2σ above the mean sky). The mean global sky background around VCC1249 was estimated and subtracted using the GALPHOT tasks MARKSKY and SKYFIT. The former allows us to mark several rectangular regions on which the sky background is estimated; the latter computes the mean sky background in each region using a sigma clipping algorithm, determines the average between the regions and subtracts this constant value from the image. The sky regions are selected to avoid the halo of M49 and other bright objects.

Because VCC1249 lies at $12^h30^m01^s.0 + 07^d55^m46^s.0$ (J2000), only 5.6 projected arcmin from M49 (see Fig.1), it is difficult to derive accurate photometry of this galaxy and its star-forming regions from the optical images, (in particular in the reddest filters) without first removing the contamination from the halo of the nearby giant elliptical. We therefore subtracted the best-fit model of the M49 light distribution from the sky-subtracted images, which we obtained for each filter (u, g, i, z)

Space Telescope Science Institute, which is operated by the Association of Universities for Research in Astronomy (AURA), Inc., under NASA contract NAS 5-26555.

⁴ Developed for DS9 by the High Energy Astrophysics Division of SAO.

⁵ https://www.astrosci.ca/NGVS/The_Next_Generation_Virgo_Cluster_Survey/Home.html

**Fig. 3.** RGB cutouts of the regions C1 (left), C2 (center), C6 (right) obtained combining the u, g, z NGVS images. At the GALEX resolution of > 4 arcsec, C1 and C2 are unresolved in the UV. The size of each image is about $10'' \times 10''$.

using in sequence the tasks ELLIPSE and BMODEL after masking VCC1249, the star-forming regions, and the bright stars. Panels (a) and (b) of Figure 2 show the RGB image before and after the subtraction of M49. To assess the quality of this subtraction, we analyzed in each subtracted image the background level in circular rings centered at the position of M49, finding no residual flux within the uncertainty of the sky level.

After removing the contamination from M49, we performed aperture photometry on the individual star-forming regions that are marked in Figure 2. The flux was measured in circular regions of about 3 – 4 arcsec in radius, subtracting the local background determined within concentric annular regions of 5 to 10 arcsec in radius. Throughout this work, we assume the nomenclature introduced by Lee et al (1997). Notice the presence of other fainter blue features near the listed HII regions (see panel (d) Figure 2), likely low surface brightness star-forming filaments or knots related to the interaction studied. Owing to their faintness and uncertain flux, these will not be further analyzed. For VCC1249 we also measured the surface brightness profile in each band (after masking the foreground stars and the background objects), using a modified version of the ELLIPSE task in IRAF that fits elliptical isophotes. For consistency we performed the ellipse-fit on the g -band image and used the same elliptical isophotes for the other bands. During the analysis of the g -band image we maintained as free parameters the ellipse center, the ellipticity, and the position angle, and incremented

the ellipse semi-major axis by 5 arcsec at each step of the fitting procedure.

2.2. UV imaging: GUViCS

The system of VCC1249 and M49 was observed by GALEX in the NUV (1750-2750 Å) as part of the GUViCS⁶ survey with an exposure time of 1630 sec. The NUV image, shown in Figure 4, reveals patchy extended emission between VCC1249 and M49. Compact emission is also seen in correspondence to some of the external HII regions. A shorter 104 sec exposure is available in the far-ultraviolet (FUV) band (1350-1750 Å) from the GALEX all-sky survey. Owing to the shallower exposure, only VCC1249 and the brightest outlying HII regions (C1, C2, C6 and C8) are marginally detected in the smoothed data. Because of the lower resolution of GALEX (> 4 arcsec), regions C3, C5, and C7 are not detected in the UV images. Furthermore, some regions that are unresolved at the GALEX resolution (e.g. C2) appear to be blends of two or more distinct HII regions resolved in the optical imaging (Figure 3). C1 is resolved into three components, one of which might be a background galaxy based on its red colors.

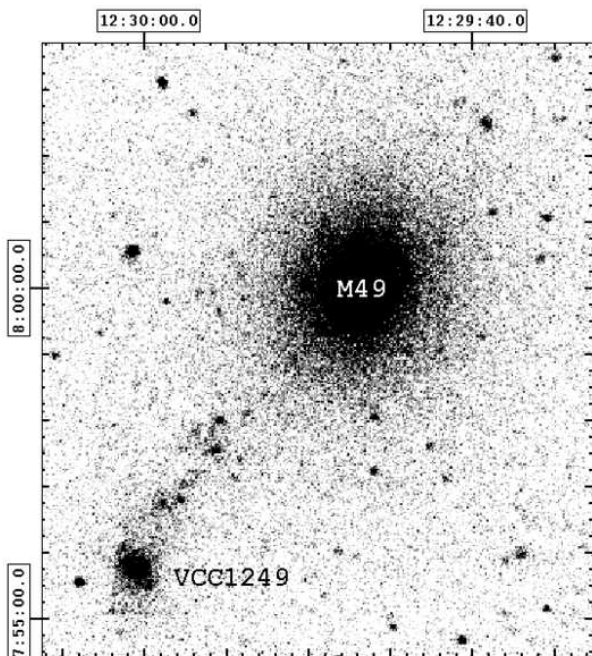


Fig. 4. NUV image of VCC1249 and M49 obtained from GUViCS. Multiple HII regions are trailing in the northeast direction from VCC1249.

Similarly to what was done for the optical imaging, we performed aperture photometry for the galaxy and the outlying HII regions. Owing to the lack of deep IR data, the internal dust extinction for VCC1249 is unknown. The IRAS 60 and 100 micron upper-limits (GoldMine⁷) imply that $A(FUV)$ is lower than ~ 2 mag (Cortese et al. 2008). Moreover, the observed UV-optical colors of this galaxy are typical of blue-sequence dwarf galaxies (Boselli et al. 2008a; Cortese & Hughes 2009), suggesting that the amount of dust absorption is likely modest (< 1

mag). We tested the robustness of our results against the adopted value of dust attenuation, finding that our analysis is not affected if $A(FUV) < 2$. Thus, for simplicity, we assume $A(FUV)=0$ throughout this paper. For the HII regions instead we estimated the dust obscuration using the Balmer decrement. Because the measured $I(H\alpha)/I(H\beta)$ ratio is 2.66 and 2.93 for C2 and C6, respectively, consistent with the expected Balmer ratio of 2.86 (case B for $T = 10000$ K; Osterbrock 1989), no correction was applied.

2.3. $H\alpha$ imaging

A 3×600 sec narrow band $H\alpha$ image was acquired with the SPM⁸ 2.12m telescope in April 2011 (see Table 1). These new data were combined with a 4×300 sec exposure acquired with the same instrument in 2001 that is available from the Goldmine database. A detailed description of the data reduction procedures for $H\alpha$ images can be found in Boselli & Gavazzi (2002), and it is only briefly summarized here. The ON-band frame was obtained using a narrow band (80 Å) filter centered at 6603 Å that overlaps with the $H\alpha$ emission line. The OFF-band frame, needed to subtract the stellar continuum, was acquired in a shorter exposure using the Gunn r -band filter. After bias subtraction and flat-fielding, the OFF band image was renormalized to match the ON-band exposure. Finally, the OFF-band was subtracted from the ON-band to obtain the image of the continuum-subtracted NET $H\alpha$ emission. The resulting NET and ON-band frames are shown in Figure 5. Although the normalization factor was determined assuming that no $H\alpha$ flux should be found associated to stars in the field, some residual flux from the brightest stars in the field appears in the NET frame due to slight differences in seeing between the OFF and ON observations (see Figure 5). The absolute flux calibration was performed with repeated exposures of the standard spectrophotometric stars Feige34 and Hz44.

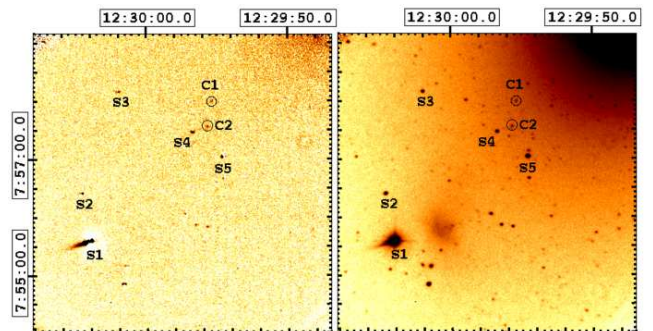


Fig. 5. $H\alpha$ image of VCC1249 and the outlying HII regions obtained at the SPM telescope. Left: $H\alpha$ net emission line. Right: $H\alpha$ plus stellar continuum frame HII regions C1 and C2 are labeled. Stars with apparent residual NET emission (see text) are labeled S1 to S5. Note the lack of substantial emission from VCC1249.

In the final image, two sources (C1 and C2) with an $H\alpha$ surface brightness higher than $\sigma_{min} = 2.0 \times 10^{-17}$ erg cm⁻² s⁻¹ arcsec⁻² were detected (5σ above the background). As previously, we measured the flux in circular apertures obtaining

⁶ <http://galex.oamp.fr/guvics/>

⁷ Gavazzi et al. (2003), Galaxy On Line Database Milano Network (<http://goldmine.mib.infn.it>)

⁸ Observatorio Astronómico Nacional en San Pedro Mártir, Baja California, Mexico.

$(8.68 \pm 0.33) \times 10^{-16} \text{ erg cm}^{-2} \text{ s}^{-1}$ and $(1.49 \pm 0.04) \times 10^{-15} \text{ erg cm}^{-2} \text{ s}^{-1}$ for C1 and C2, respectively. Since the narrow band filter is broad enough to include the bracketing [NII] lines, the listed $H\alpha$ fluxes were corrected accordingly, using $[NII]/H\alpha = 0.11$ for C2, as measured on the spectrum, while for C1 we used an average ratio of about 0.1, as derived from the spectra of C2 and C6.

2.4. Spectroscopy

We observed the HII regions C2⁹, C4, and C6 on UT 2011 January, 3 and 4 with the LRIS spectrograph (Oke et al, 1995) at the Keck I telescope on Mauna Kea. During the first night we obtained 2×1200 sec exposures of C2 and C4, using a $1''$ slit and with the instrument configured with the 600/4000 grism, the D560 dichroic and the 600/7500 grating, tilted to ensure continuous spectral coverage between the blue and red arms. A single exposure of 900 sec was obtained during the second night, with a similar configuration but using the 400/3400 grism. The 2D images were reduced with the LowRedux pipeline¹⁰, which calibrates, extracts and fluxes the data. C1 was subsequently observed on the UT night 2011 April, 29 with the KAST spectrograph at the Lick observatory. We obtained 2×1800 sec exposures with the 600/4310 grism, the 600/7500 grating and the D55 dichroic using a $2''$ slit. For regions C12 and C17 the spectra taken in $3''$ apertures were retrieved from SDSS.

3. Properties of VCC1249

VCC1249 is a dIrr (Nilson et al. 1973) low-surface brightness galaxy, located 5.6 arcmin to the southeast of the giant elliptical galaxy M49 (Kumar & Thonnard 1983), the brightest member of Virgo Cluster B, approximately 4 degrees (1.19 Mpc projected distance) south of M87 (Virgo Cluster A). VCC1249 has an irregular morphology: the central part of the galaxy consists of several bright knots connected by bridges (Lee et al. 1997) and from this structure a tidal tail departs toward M49 in the northwest direction and a counter tail in the southwest direction (Patterson & Thuan 1992 and McNamara et al. 1994; see Figure 2). Based on its photometric properties (Table 2), VCC1249 is a dwarf galaxy that lies in the blue cloud of the color-magnitude diagram of the Virgo cluster galaxies.

VCC1249 has a systemic velocity of $390 \pm 30 \text{ km s}^{-1}$ (SDSS)¹¹, while M49 has $1001 \pm 12 \text{ km s}^{-1}$ (Schechter 1980). An HI cloud with $M_{HI} = (6.9 \pm 0.4) \times 10^7 M_{\odot}$ and radial velocity of 469 km s^{-1} (McNamara et al. 1994), in agreement with the previous measurement of $472 \pm 4 \text{ km s}^{-1}$ (Sancisi et al. 1987), belonging to VCC1249 and displaced toward M49, is detected in 21-cm (see Figure 6). Conversely, VCC1249 itself shows no significant emission in the hydrogen line to a limit of $M_{HI} < 4.2 \times 10^7 M_{\odot}$ (Oosterloo & Shostak 1984). Quantified in terms of the HI deficiency (def_{HI}), defined as the logarithmic difference between the upper limit HI mass and the expected value for a galaxy of the same morphological type and size (Haynes & Giovanelli 1984), VCC1249 has $def_{HI} > 0.92$ and is among the most deficient

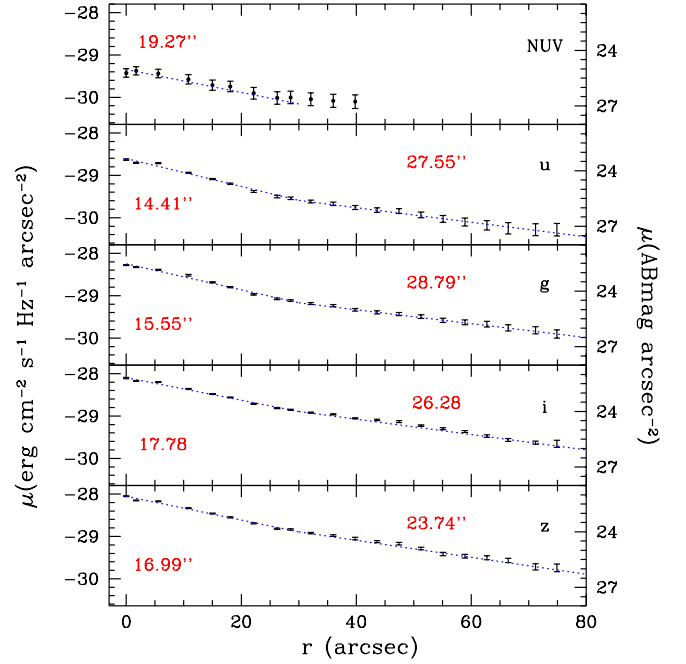


Fig. 7. Surface brightness profile of VCC1249, obtained using ELLIPSE, letting the center, the ellipticity, and the position angle as free parameters. In red, we show the inner and outer scale lengths computed for each band adopting a two-component exponential profile (superimposed in blue). $r = \sqrt{a \cdot b}$, where a and b are the semi-major and the semi-minor axis of the isophotal ellipses, respectively.

galaxies in the local Universe. This is not particularly surprising, since at the projected distance between M49 and VCC1249 of about 30 kpc, the X-ray emission is dominated by the hot (10^7 K Forman et al. 1985) gas belonging to the halo of M49 with a density of more than 10^{-3} cm^{-3} (Fabian 1985).

In Figure 7 we show the surface brightness profile of VCC1249 as a function of the radius $r = \sqrt{a \cdot b}$, where a and b are the semi-major and the semi-minor axis of the isophotal ellipses, respectively. The profiles are well fitted by an exponential law with two components (for $0'' < r < 30''$ and $30'' < r < 80''$). The first component is characteristic of a disk, while the second one accounts for the presence of the tidal tail and its counter-tail (Patterson & Thuan 1992; Lee et al. 1997), which appear as an excess of light above the inner exponential fit, resulting in a greater scale length in the outer part of the profile.

The color profiles of VCC1249 are shown in Figure 8. The $u - i$ and $g - i$ indices are as blue as $u - i = 1.20$ and $g - i = 0.39$ near the center, become redder moving outward up to 20 arcsec, then they flatten, consistently with the results of Lee et al. (1997) and Patterson & Thuan (1996). However, the $NUV - u$ color shows an opposite trend: from $NUV - u = 1.8$ near the center to 0.8 at 40 arcsec. Note, however, that the uncertainties in these colors are large.

Inspecting our $H\alpha$ imaging, we see a lack of significant $H\alpha$ emission associated to VCC1249 and to its tidal tails. Using an upper limit of $F_{H\alpha}^{VCC1249} < 3.80 \times 10^{-14} \text{ erg cm}^{-2} \text{ s}^{-1}$, we infer an upper limit to the star formation rate (SFR) of about $< 0.01 M_{\odot} \text{ yr}^{-1}$, using the calibration of Kennicutt (1998). Because $H\alpha$ traces massive star formation, the lack of signifi-

⁹ LR1 in Lee et al. 2000

¹⁰ <http://www.ucolick.org/xavier/LowRedux/index.html>

¹¹ This is the redshift reported by SDSS for regions C12 and C17. Huchra (1992) found $276 \pm 78 \text{ km s}^{-1}$. Using this value, the relative velocity between VCC1249 and M49 would increase and the ram pressure would appear more effective. In turn, this would lead to a more rapid removal of the gas ($58 \pm 21 \text{ Myr}$), leaving our conclusions unchanged, however.

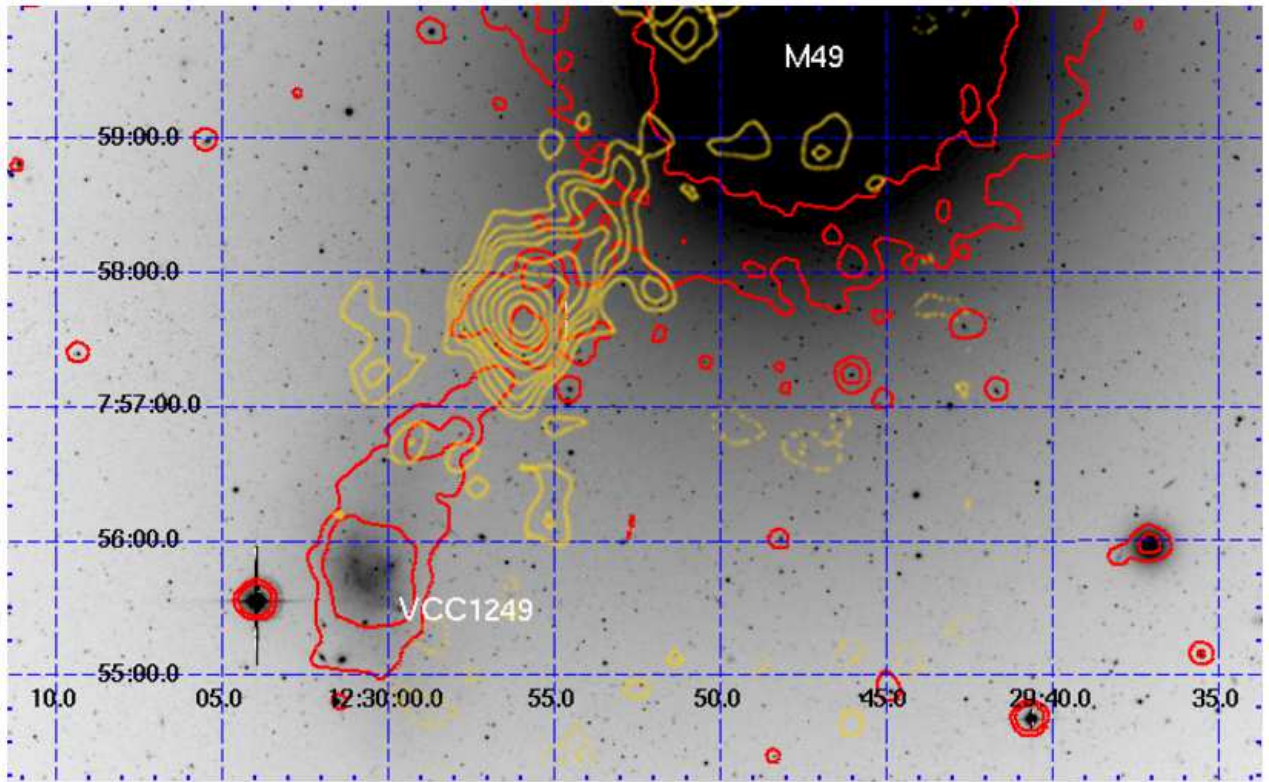


Fig. 6. NGVS *g* image of VCC1249 (bottom-left) and of M49 (top-center) on which the NUV contours (red) and the HI contours taken from McNamara et al. (1994) (yellow) are superposed (the coordinates are precessed from B1950 originally used, to J2000). Note that the peak of the HI cloud nearly coincides with the peak of the NUV emission at the position of the region C2 (LR1 in Lee et al. 2000).

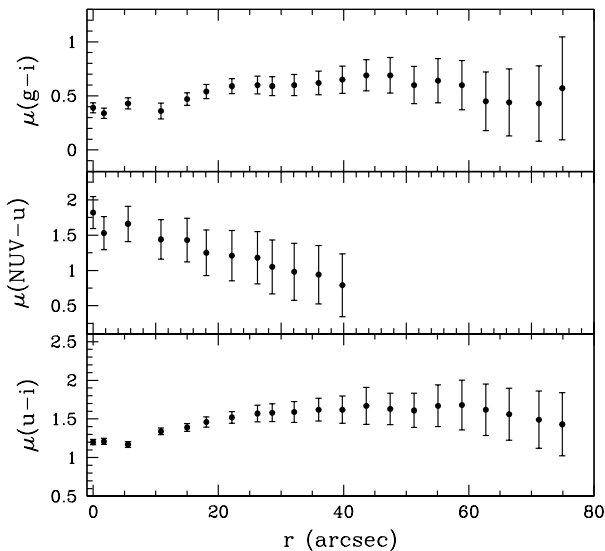


Fig. 8. Color profile of VCC1249, obtained from the surface brightness profiles in Figure 7.

cant H α emission sets an upper limit on the age of the last star-formation event at ≥ 20 Myr, i.e. the typical life-time of mas-

sive stars. Using the FUV emission instead, we infer an SFR of about $0.005 \pm 0.001 M_{\odot} \text{ yr}^{-1}$ following Kennicutt (1998). The presence of far-ultraviolet continuum indicates that star formation occurred ≥ 100 Myr ago, which combined with the lack of H α emission, suggests that the star formation in VCC1249 was truncated recently.

4. Properties of the external star-forming regions

4.1. Morphology and photometry

A complex of star-forming regions extends from the galaxy in northwest direction, up to 2.6 arcmin (about 13 kpc) far from VCC1249, as clearly visible from both the GALEX images and the NGVS images (Figure 2a,b).

Figure 9 shows the $NUV - u$ colors of these star-forming regions compared to VCC1249. It appears that all the structures outside VCC1249 are much bluer than the galaxy ($NUV - u = 1.86$ and $u - i = 1.41$). C12 and C17, belonging to the central region of VCC1249, are unresolved in the UV images and appear redder in the $u - i$ color than all other regions, having $(u - i)_{C12} = 1.06$ and $(u - i)_{C17} = 1.91$, respectively. Conversely, the other regions have a mean color of $\langle NUV - u \rangle = -0.29$ and $\langle u - i \rangle = 0.21$. Only region C7 is as red as the regions belonging to the galaxy in $u - i$, but visual inspection of the imaging suggests that this is probably due to contamination from a background red source (see Figure 2). Furthermore, the lack of a clear dependence of these colors as a function of the projected distance from the galaxy suggests that these regions are nearly coeval, regardless of the galactocentric distance.

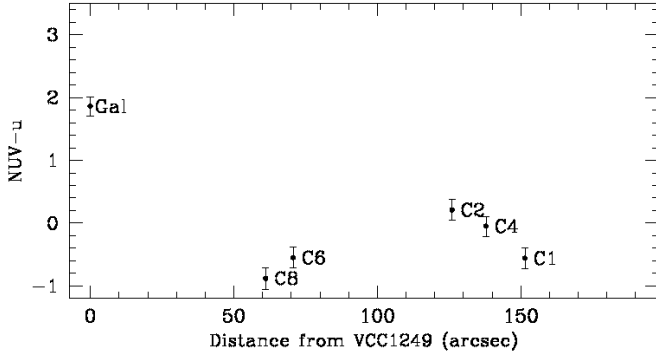


Fig. 9. $NUV-u$ color of the studied HII regions and of VCC1249 itself as a function of the projected distance from VCC1249. All outlying HII regions are bluer than VCC1249.

Only regions C1 and C2 display $H\alpha$ emission at the depth of our imaging. Their luminosities are $2.78 \times 10^{37} \text{ erg s}^{-1}$ and $4.78 \times 10^{37} \text{ erg s}^{-1}$, respectively, consistent with the faint end of the HII luminosity function (Kennicutt et al. 1989). Adopting the Kennicutt (1998) conversion, the inferred SFR is $2.20 \times 10^{-4} M_{\odot} \text{ yr}^{-1}$ (C1) and $3.77 \times 10^{-4} M_{\odot} \text{ yr}^{-1}$ (C2). Using the FUV emission instead, we compute an SFR of about $(7 \pm 2) \times 10^{-4} M_{\odot} \text{ yr}^{-1}$ and $(6 \pm 2) \times 10^{-4} M_{\odot} \text{ yr}^{-1}$, for C1 and C2, respectively. The SFR of the other regions can be estimated from the FUV luminosity to approximately $10^{-4} M_{\odot} \text{ yr}^{-1}$ per region (see Table 7)¹².

4.2. Radial velocities and line properties

The Keck spectra of C2 and C6 are shown in Figure 10, where we highlight the detected emission lines. These two spectra have a mean signal-to-noise ratio (S/N) of 3.7 and 2.2¹³, respectively. The lower S/N in the spectra for the fainter HII regions C4 and C1, 0.9 and 1.4, respectively, prevented a detailed study of their emission properties, but we can derive an estimate of the radial velocity from the marginally detected $H\alpha$ lines. Since the measured $I(H\alpha)/I(H\beta)$ ratio is about 2.66 and 2.93 for C2 and C6, respectively, consistent with the expected Balmer ratio of 2.86 (case B for $T = 10000 \text{ K}$; Osterbrock 1989) within the uncertainty, no reddening correction was applied to the spectra.

We computed the radial velocities of C2 and C6 by averaging the redshift measurements obtained from the individual spectral lines. C2 and C6 have a radial velocity of $561 \pm 34 \text{ km s}^{-1}$ and $533 \pm 53 \text{ km s}^{-1}$, respectively. Our redshift measurement for C2 agrees with the value $577 \pm 91 \text{ km s}^{-1}$ from Lee et al. (2000). The radial velocities listed in Table 3 systematically increase toward M49 ($1001 \pm 12 \text{ km s}^{-1}$). HI interferometric observations carried out with the VLA have shown that regions C1-C5 are apparently associated with an HI cloud of $\approx 6.9 \times 10^7 M_{\odot}$ at a recessional velocity of 469 km s^{-1} extending over 20 km s^{-1} (McNamara et al. 1994). The VLA channel maps show a velocity gradient across the HI cloud: the material in the northwest part has higher velocities ($10\text{-}15 \text{ km s}^{-1}$) compared to the center (McNamara et al. 1994). Having a bandpass of about 330 km s^{-1} centered at 470 km s^{-1} , these observations (as well as the WSRT observation by Henning et al. 1993) cannot be used to check if

¹² The Kennicutt (1998) calibration applies to continuous star formation over 10^8 yr or longer. Therefore, the estimated SFR of the HII regions should be approached with some caution.

¹³ Obviously, the S/N turns out to be much higher in correspondence of the lines, exceeding 10 for the C2 and C6 regions.

the association on the plane of the sky is also present in the velocity space. Lower resolution WSRT observations (Sancisi et al. 1987) and Arecibo observations (Hoffman et al. 1987) covering a broader range in the velocity space, however, do not detect any 21 cm emission with an rms of 0.7 mJy at the redshift of C1 or C4, and probably C2 and C6 (see Table 3).

Table 3. Radial velocities for C1, C2, C4, C6, C12, and C17.

Region	Proj. Dist. (kpc)	Velocity (km s ⁻¹)
(VCC1249)	0	390 ± 30
C12	0.5	390 ± 30
C17	1.5	390 ± 30
C6	5.6	533 ± 53
(HI)	10.0	469 ± 3
C2	10.0	561 ± 34
C4	11.0	656 ± 73
C1	12.0	716 ± 106
(M49)	26.5	1001 ± 12

The observed equivalent widths (EW) of the lines measured in C2 and C6 (adopting the convention that negative EW means emission) are listed in Table 5. From the ratios $[OIII] \lambda 5007/H\beta$ and $[NII] \lambda 6584/H\alpha$, we determine that, as expected, C2 and C6 lie on the HII regions arm of the BPT diagram (Baldwin et al. 1981). No clear features related to shocks are seen in the spectra: no strong $[OI]$ line is detected and all diagnostic ratios (involving $[OI]$, $[OIII]$, $H\beta$, $H\alpha$, $[SII]$, $[NII]$ lines) agree with the photo-ionization models that place C2 and C6 among HII regions (see e.g. Dopita & Evans 1986).

Conversely, the SDSS spectra of C12 and C17 belonging to VCC1249 exhibit no emission lines, but clearly show Balmer lines in absorption. In Table 4 we report the line equivalent widths. Consistent with our analysis of the star formation rate properties, the observed values are typical of k+a galaxies ($EW(H\delta) > 3 \text{ \AA}$, Poggianti et al. 2004, Dressler et al. 1999), post star-burst (PSB) galaxies whose star formation has been suddenly truncated. These characteristics are not only found in C12 and C17, but are representative of the entire galaxy. Indeed, the spectrum of VCC1249 (Patterson & Thuan 1992; Huchra 1992) exhibits no emission lines and strong $H\beta$ in absorption.

Table 4. The Balmer absorption lines of C12 and C17.

	Wavelength (Å)	EW (C12) (Å)	EW (C17) (Å)
H δ	4101.7	5	4
H γ	4339.8	6	2
H β	4861.0	5	4
H α	6562.8	1	7

4.2.1. Metallicity

Since the $[OIII] \lambda 4363$ line is undetected in the spectra of C2 and C6, we determined the oxygen abundances using the strong line methods. Several such methods, based on different line ratios with empirical, theoretical or "combined" calibrations, can be found in the literature.

Since the abundances derived using these indirect methods are affected by up to ~ 0.7 dex uncertainties (Kewley & Ellison

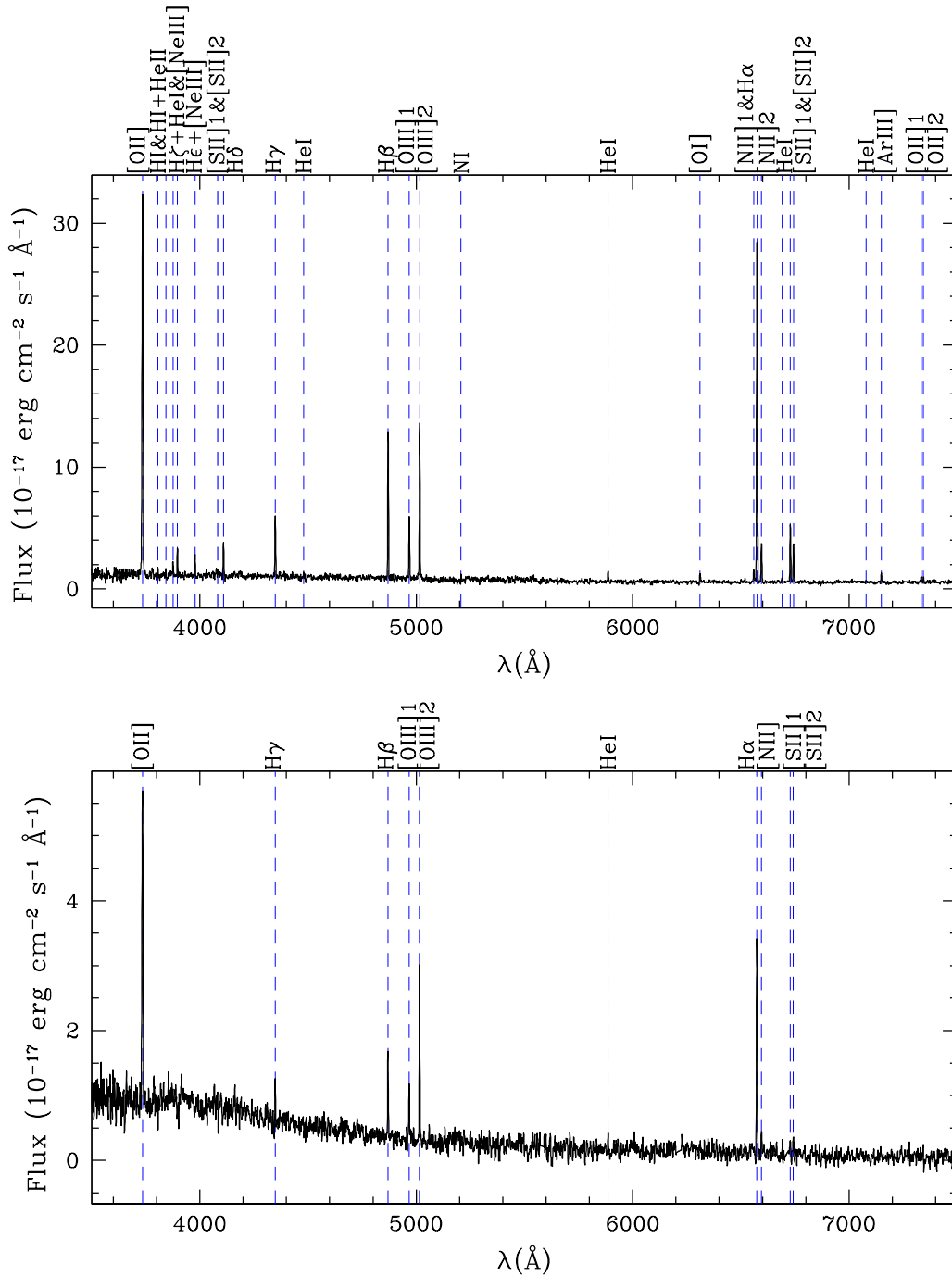


Fig. 10. Spectrum of the HII regions C2 (top) and C6 (bottom) obtained at Keck. Dashed lines highlight the position of the lines in Table 5.

2008), we calculated the chemical composition of the HII regions C2 and C6 using multiple ratios of strong lines¹⁴. For the R_{23} method, the observed $\log([NII]/H\alpha) > -1.1$ puts C2 and C6 in the upper branch.

¹⁴ $R_{23} = ([OII] \lambda 3727 + [OIII] \lambda 4959, 5007) / H\beta \lambda 4861$, $O_{23} = ([OIII] \lambda 4959 + [OIII] \lambda 5007) / [OII] \lambda 3727$, $[NII] \lambda 6584 / H\alpha \lambda 6563$, $[OIII] \lambda 5007 / [NII] \lambda 6584$, $[NII] \lambda 6584 / [OII] \lambda 3727$, and $[NII] \lambda 6584 / [SII] \lambda 6720$

Then, following the procedure of Kewley & Ellison (2008), we homogenized the derived values to the Pettini & Pagel (2004) calibration to remove any systematic discrepancy between the various calibrations. The abundances derived using several calibrations, before and after this conversion, are listed in Table 6. The inferred oxygen abundances show a peak to peak variation of $\sim 0.2 - 0.3$ dex. By averaging these different values, we obtained our best estimate of the metallicity $12 + \log(\frac{O}{H}) = 8.38$ for C2 and $12 + \log(\frac{O}{H}) = 8.29$ for C6.

Table 5. Summary of the emission lines detected in the HII regions C2 and C6

	C2				C6		
	λ (rest) (Å)	λ (observed) (Å)	Log Continuum (erg cm ⁻² s ⁻¹ Å ⁻¹)	EW (Å)	λ (observed) (Å)	Log Continuum (erg cm ⁻² s ⁻¹ Å ⁻¹)	EW (Å)
[OII]	3727.55	3735.2	-16.93	-148.9 ± 1.1	3734.8	-17.04	-29.5 ± 0.8
HI	3798	3805.9	-16.95	-1.7 ± 0.4	-	-	-
HI+HeII	3834	3842.4	-16.95	-1.4 ± 0.5	-	-	-
[NeIII]	3868.7	3876.2	-16.95	-3.9 ± 0.4	-	-	-
Hζ+HeI	3888.9	3896.4	-16.96	-7.3 ± 0.4	-	-	-
Heε + [NeIII]	3970.1	3977.6	-16.97	-6.3 ± 0.3	-	-	-
[SII]1	4070	4082.9	-16.93	-0.7 ± 0.3	-	-	-
[SII]2	4078	4087.1	-16.93	-0.9 ± 0.3	-	-	-
Hδ	4101.7	4109.6	-16.95	-9.8 ± 0.5	-	-	-
Hγ	4339.8	4348.7	-16.98	-19.8 ± 0.6	4348.3	-17.21	-3.4 ± 0.5
HeI	4471.5	4480.0	-17.02	-1.5 ± 0.4	-	-	-
Hβ	4861.0	4870.2	-17.06	-57.2 ± 0.6	4869.4	-17.43	-13.6 ± 0.9
[OIII]1	4958.9	4967.9	-17.06	-24.5 ± 0.6	4967.3	-17.49	-10.6 ± 1.1
[OIII]2	5006.8	5015.8	-17.07	-62.4 ± 0.8	5015.2	-17.52	-34.3 ± 1.2
NI	5199	5207.4	-17.17	-2.4 ± 0.6	-	-	-
HeI	5875.6	5886.3	-17.23	-6.6 ± 0.7	5886.5	-17.82	-5.9 ± 2.7
[OI]	6300.3	6311.7	-17.25	-5.9 ± 0.6	-	-	-
[NII]1	6548.1	6559.8	-17.28	-9.7 ± 0.6	-	-	-
Hα	6562.3	6574.8	-17.28	-252.9 ± 1.0	6574.1	-17.89	-115.2 ± 1.5
[NII]2	6583.4	6595.5	-17.28	-28.8 ± 0.5	6595.3	-17.89	-10.8 ± 2.1
HeI	6678	6690.5	-17.25	-3.2 ± 0.5	-	-	-
[SII]	6717	6728.8	-17.25	-38.8 ± 0.6	6727.9	-18.00	-11.4 ± 2.7
[SII]	6731.3	6743.1	-17.25	-25.7 ± 0.6	6742.6	-18.05	-17.1 ± 1.9
HeI	7065	7078.4	-17.26	-0.9 ± 0.4	-	-	-
[ArIII]	7135.8	7149.1	-17.28	-6.3 ± 0.5	-	-	-
[OII]1	7319.5	7333.5	-17.27	-4.0 ± 0.4	-	-	-
[OII]2	7330.5	7344.1	-17.27	-3.0 ± 0.6	-	-	-

Table 6. Oxygen abundances of the HII regions C2 and C6. The values converted to the Pettini & Pagel (2004) calibration are given in parenthesis.

Ratio	C2	C6	Calibration
	$12 + \log\left(\frac{O}{H}\right)$	$12 + \log\left(\frac{O}{H}\right)$	
R_{23}, O_{32}	8.69 (8.49)	8.41 (8.34)	McGaugh (1991)
$\frac{[NII]}{[OIII]}$	8.45 (8.24)	-	Kewley & Dopita (2002)
R_{23}, O_{32}	8.85 (8.48)	8.50 (8.19)	Kobulnicky & Kewley (2004)
R_{23}	8.81 (8.49)	8.74 (8.42)	Zaritsky et al. (1994)
$\frac{[NII]}{H\alpha}$	8.31	8.25	Pettini & Pagel (2004)
$\frac{[NII]}{H\alpha}$	8.43 (8.31)	8.35 (8.25)	Denicoló et al. (2002)

Assuming a solar abundance $12 + \log\left(\frac{O}{H}\right) = 8.69$ (Asplund et al. 2009), these values imply a subsolar metallicity in these two regions ($Z = 0.49Z_{\odot}$ for C2 and $Z = 0.40Z_{\odot}$ for C6). Remarkably, this value is consistent with the metallicity derived for VCC1249 itself using the mass metallicity relation (see subsection 5.1), which strengthens the hypothesis that the external HII regions were born in situ from the pre-enriched gas that has been stripped from VCC1249.

5. SED fitting

To constrain the star formation history of VCC1249 and its HII regions, we used the SED fitting technique presented in Fumagalli et al. (2011). First, using the spectrophotometric evolution code PEGASE2.0¹⁵, we created a grid of synthetic spectra evaluated at different times for multiple input star formation histories SFR(t). Then, using the SED-fitting code GOSSIP (Franzetti et al. 2008), we compared the observed photometric points (and spectra if available) with the synthetic spectra. During this procedure, we analyzed VCC1249, M49, and the HII regions separately.

5.1. The galaxy (VCC1249)

As in Fumagalli et al. (2011), the evolution of the spectral energy distribution of the galaxy was modeled assuming a Salpeter IMF, with a lower mass end of $0.1 M_{\odot}$ and an upper mass of $120 M_{\odot}$. Initially, we assumed zero metallicity, then the ejecta of massive stars (Woosley & Weaver 1995), implemented in the PEGASE code, enrich the ISM¹⁶. Furthermore, we assumed a delayed exponential star formation history, dubbed “a la Sandage” (see equation 3 in Gavazzi et al. 2002, Sandage 1986), truncated as in Fumagalli et al. (2011) to simulate the stripping event on

¹⁵ Projet d’Etude des GALaxies par Synthèse Evolutive.

¹⁶ PEGASE uses the “Padova” stellar tracks, improved with the AGB phase (Groenewegen & de Jong 1993) and with the helium white dwarfs (Althaus & Benvenuto 1997). See <http://www2.iap.fr/users/fioc/PEGASE.html> for more details.

VCC1249 due to the interaction with M49. Analytically, this is

$$\text{SFR}(t) = \begin{cases} \frac{t}{\tau^2} e^{-\frac{t^2}{\tau^2}} & \text{if } t < t_{\text{trunc}} \\ 0 & \text{if } t > t_{\text{trunc}} \end{cases}$$

where t_{trunc} is the time from the onset until the end of star formation activity.

In Figure 11 (adapted from Fumagalli et al. 2011), we show an example of star formation history from our model library and we highlight the various timescales that are relevant for this analysis.

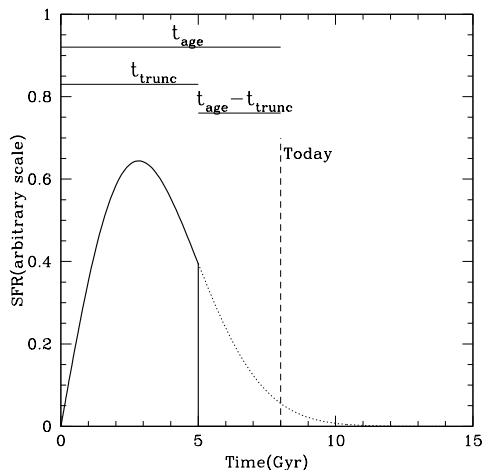


Fig. 11. Example of star formation history from our library, with $\tau=4$ Gyr, $t_{\text{age}}=8$ Gyr and $t_{\text{trunc}}=5$ Gyr (adapted from Fumagalli et al. 2011).

In this grid of synthetic spectra, the characteristic time scale of the burst τ ranges from 1 to 20 Gyr with steps of 1 Gyr. The age of truncation t_{trunc} varies from 1 to 13 Gyr with steps of 1 Gyr, while t_{age} spans from 0 to 13.5 Gyr with steps of 100 Myr. Our final library includes 35K spectra. During the fit, we did not fix the age for the onset of star formation activity and, as previously discussed, we did not include the (unknown) dust correction, since extinction is expected to be negligible for VCC1249 (see figure 8 of Cortese et al. 2008 and 3-4 of Lee et al. 2009).

With this library, we ran the GOSSIP software to evaluate the parameters that best reproduce the observed photometry and their associated probability distribution functions (PDFs). For VCC1249, we found that t_{age} , t_{trunc} , and τ are not well constrained individually and we were only able to constrain the two latter parameters to be < 2 Gyr. Conversely, the parameter $t_{\text{age}} - t_{\text{trunc}}$, which represents the lookback time at which the truncation of star formation occurred, is better constrained $t_{\text{age}} - t_{\text{trunc}} = 200^{+100}_{-100}$ Myr. Figure 12 shows the associated PDF. This best-fit value agrees with the PSB spectral features observed in VCC1249 that are expected to arise if the star formation activity halted abruptly in the past 0.5 – 1.5 Gyr (Couch & Sharples 1987). Furthermore, this is consistent with the observed lack of H α emission and with the presence of faint FUV emission.

Having inferred the star formation history of this galaxy, we can estimate its stellar mass by integrating the best-fit star formation history $M_{\text{star}} = (1.20 \pm 0.16) \times 10^9 M_{\odot}$. This value is consistent with what was reported by Lee et al. 2003, $M_{\text{star}} =$

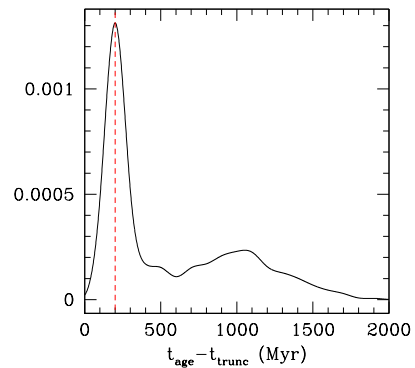


Fig. 12. Probability distribution functions of the $t_{\text{age}} - t_{\text{trunc}}$ parameter for VCC1249. The truncation of star formation appears to be well constrained at about 200 Myr ago.

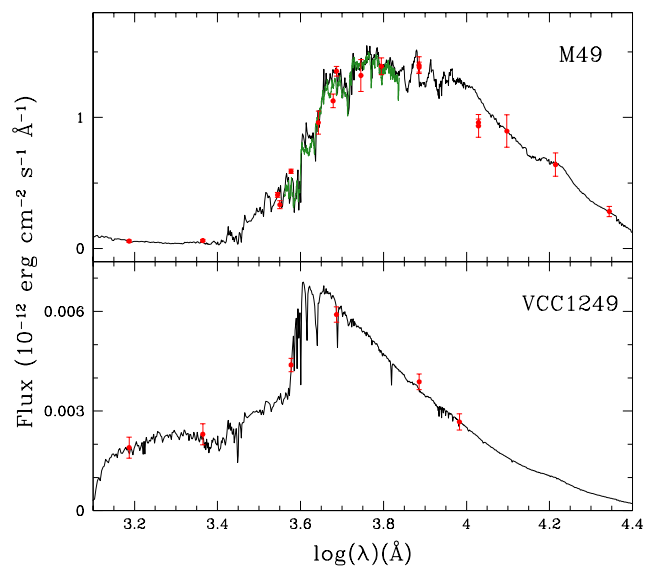


Fig. 13. Model SED for M49 (top panel) together with the observed NIR photometric points and an optical spectrum (green) from GoldMine. The best-fit model is for a Sandage star formation history with $t_{\text{age}} = 12$ Gyr and $\tau = 2.8$ Gyr. For VCC1249 instead (shown in the bottom panel), we find that a truncated Sandage star formation history with a $t_{\text{age}} - t_{\text{trunc}}$ of ~ 200 Myr provides a good description of the observed SED.

$9.55 \times 10^8 M_{\odot}$. For a $10^9 M_{\odot}$ galaxy, the mass metallicity relation (Kewley & Ellison 2008 using the Pettini & Pagel 2004 calibration) predicts $12 + \log\left(\frac{Z}{Z_{\odot}}\right) \sim 8.35$, which agrees well with the metallicity derived for C2 and C6. Again, this confirms a scenario in which the HII regions were born from the gas stripped from VCC1249 and pre-enriched by previous episodes of star formation.

Figure 13 shows the best-fit model and the SED of VCC1249 (bottom panel) and of M49 (top panel) ($\chi^2_{\text{VCC1249}} = 0.29$; $\chi^2_{\text{M49}} = 0.90$). A detailed analysis of the elliptical galaxy is be-

Table 7. Derived parameters of the HII regions. The SFR is computed from H α luminosity (left) and from FUV (right) for C1 and C2 and only from FUV for the remaining regions using Kennicutt (1998) calibrations. Mass and age are obtained from the SED fitting analysis.

Name	Proj. Dist. from VCC1249 (kpc)	Log H α Flux (erg cm $^{-2}$ s $^{-1}$)	SFR (10 $^{-4}$ M $_{\odot}$ yr $^{-1}$)	Mass (10 4 M $_{\odot}$)	Age (Myr)
C1	12.0	-15.06	2.20 \pm 0.09/7 \pm 2	1.04	4 $^{+2}_{-1}$
C2	10.0	-14.83	3.77 \pm 0.11/6 \pm 2	1.45	7 $^{+1}_{-1}$
C3	9.5	-	-	-	-
C4	11.0	-	1.7 \pm 0.7	1.36	20 $^{+30}_{-11}$
C5	12.4	-	-	-	-
C6	5.6	-	6 \pm 2	0.66	6 $^{+1}_{-1}$
C7	4.4	-	-	-	-
C8	4.9	-	7 \pm 2	2.19	10 $^{+3}_{-2}$
C12	0.5	-	-	37.15	720 $^{+520}_{-310}$
C17	1.5	-	-	17.78	2500 $^{+980}_{-980}$

yond the scope of this study, but provides a test for our fitting tools. In this case, we complemented the NGVS measurements with J,H,K,U,B,V photometry and an optical spectrum taken from GoldMine. The best fit performed adopting a star formation history “a la Sandage” and a Salpeter IMF provides $t_{age} = 12^{+1}_{-2}$ Gyr and $\tau = 2.8 \pm 1$ Gyr. Our determination agrees with the value of $t_{age} = 11.9$ Gyr found by Idiart et al. (2007) and marginally agrees with $t_{age} = 9.6 \pm 1.4$ Gyr of Thomas et al. (2005).

5.2. The star-forming regions

For the analysis of the external HII regions we performed again a modeling similar to the one presented in Fumagalli et al. (2011). First, we computed a set of synthetic spectra with PEGASE2.0, assuming a single stellar burst with Salpeter IMF and slightly subsolar initial metallicity. As justified by the observed Balmer decrement, we neglected internal dust absorption. For C12 and C17, which belong to VCC1249, we performed the SED fitting using both the single-burst model and an exponentially decreasing SFR with τ ranging from 10 to 2000 Myr.

Table 7 contains the best-fit parameters for the observed SEDs. The outlying HII regions are well described (e.g. $\chi^2_{C2} = 0.63$; $\chi^2_{C6} = 0.24$) by a single burst of star formation, with age $t < 30$ Myr. Instead, the star formation history of C12 and C17 is better described ($\chi^2_{C12} = 1.47$; $\chi^2_{C17} = 0.87$) by an exponential with $\tau < 20$ Myr and with an age about a factor of 100 higher than that of the HII regions outside the galaxy, such as C2 or C1. This result is consistent with the mean ages of $\approx 10^7$ yr and 10^8 yr obtained by Lee et al. (1997) assuming the $(B - V)$ -age relation given by Bruzual & Charlot (1993).

Figure 14 shows the SEDs of the regions, along with the PDFs of the age parameter that appears to be well constrained. As previously inferred from the lack of color variation among different HII regions (see Section 4.1 and Figure 9), our SED analysis indicates that these star-forming regions form an homogeneous population and that they are significantly different from

VCC1249 and hence from the two knots belonging to the galaxy (C12 and C17). As done previously for VCC1249, by integrating over the star formation history, we estimate the stellar masses of the studied regions to be between 0.66×10^4 and 3.72×10^5 M $_{\odot}$. These values are typically found in star cluster complexes and HII regions (Kennicutt et al. 1989).

6. Discussion

Our multiwavelength analysis of VCC1249, based on new GALEX NUV data, deep optical imaging (including H α) and Keck spectroscopy, reveals that star formation was recently quenched in this dwarf and that the only star-forming regions are those outside the main body of the galaxy, made of pre-enriched gas in the HI cloud.

These findings are consistent with the conclusions of Sancisi et al. (1987), Patterson & Thuan (1992), and Lee et al. (2000) that this dwarf has suffered from ram-pressure stripping in the hot atmosphere of M49, leading to the ablation of most of its original HI gas. Following previous calculations (Sancisi et al. 1987; Patterson & Thuan 1992) and using our newly estimated parameters, we find that VCC1249 is in fact unable to retain its gas at any radius because of ram pressure stripping. The radius at which ram pressure (Gunn & Gott 1972) becomes efficient can be estimated as (Domainko et al. 2006)

$$R_{strip} = 0.5R_0 \ln \left(\frac{GM_{star}M_{gas}}{v^2 \rho_{Halo} 2\pi R_0^4} \right), \quad (1)$$

while the stripped mass is

$$M_{strip} = M_{gas} \left(\frac{R_{strip}}{R_0} + 1 \right) \exp \left(-\frac{R_{strip}}{R_0} \right). \quad (2)$$

Here, $\rho_{Halo} = 10^{-3}$ cm $^{-3}$ is the gas density in the halo of M49 (Fabian 1985) and $v = 611 \pm 32$ km s $^{-1}$ is the relative velocity between VCC1249 and M49. In this calculation we furthermore

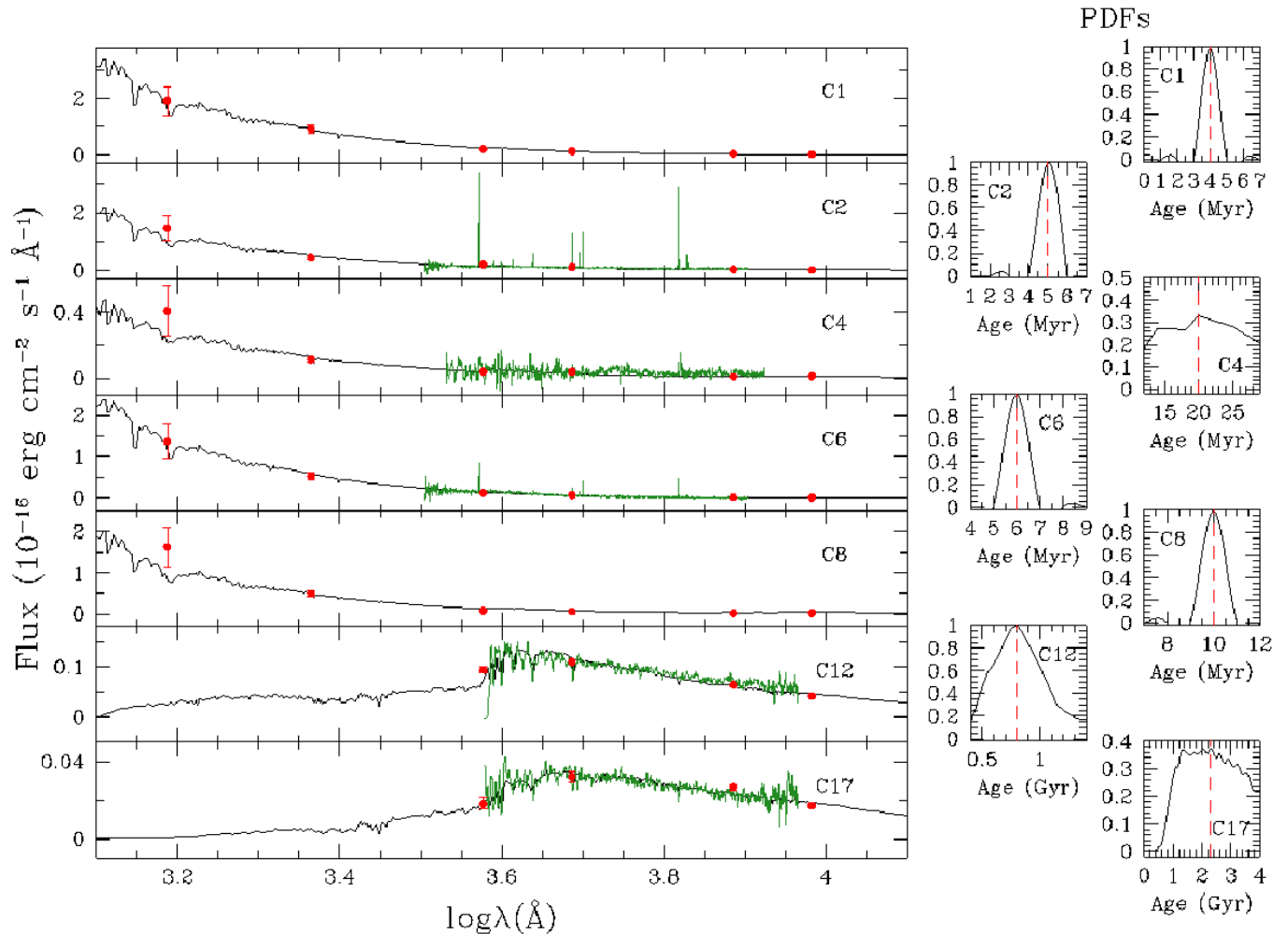


Fig. 14. Summary plot of the photometric points for the HII regions (red), observed optical spectrum if available (green) and their best-fit SEDs. Data for C1, C2, C4, C6, and C8 have been modeled using a single burst, while C12 and C17 using an exponentially declining SFR. The probability distribution functions for the age parameter of each individual region are shown in the right panels.

assumed an exponential profile for the stellar and gas components, with $R_0 = 14.5$ arcsec, the inner scale length computed in Section 3 using the g -band luminosity. Adopting $M_{star} = 1.20 \times 10^9 M_\odot$, $M_{gas} = 8.41 \times 10^7 M_\odot$ (since $M_{gas} - M_{strip} = 1.51 \times 10^7 M_\odot$, Lee et al. 2003), we find that VCC1249 cannot retain its gas at any radius, accordingly $M_{strip} = M_{gas}$. Ram-pressure stripping can therefore fully deplete the gas reservoir of this dwarf, leading to a sudden truncation of its star formation¹⁷.

However, as pointed out by Patterson & Thuan (1992) and McNamara et al. (1994), ram-pressure stripping is not the only mechanism acting on this system because, for instance, it cannot explain the presence of the tail and counter-tail of VCC1249 (Fig. 2b,c). These features instead naturally arise from a tidal interaction with M49. Patterson & Thuan (1992) estimated that the tidal radius, i.e. the distance at which stars in VCC1249 become unbound or stripped, is > 20 arcsec, in agreement with the excess of light superimposed to the inner exponential profile that

is visible in our deep optical profiles. We conclude therefore that both ram pressure and tidal interaction occurred during the interaction with M49: gravitational tides triggered the tail and the counter-tail of VCC1249 and aid ram pressure to remove the HI gas by diminishing the overall potential of the dwarf.

Furthermore, using our SED analysis, we can estimate the epoch of the encounter between VCC1249 and M49. Our best-fit model for the SED requires a sudden truncation of the star formation activity 200 Myr ago because of gas ablation. This time is also consistent with an independent estimate for the ablation time derived by dividing the projected distance between the HI cloud and VCC1249 (about 10 kpc) by their relative radial velocities ($\Delta V = 79 \pm 30 \text{ km s}^{-1}$). Neglecting projection effects, this very crude calculation shows that $\sim 124 \pm 47$ Myr are needed to displace the gas from VCC1249 to the location where it is detected in the 21 cm emission.

Focusing on the outlying HII regions, both the SED fitting and the spectroscopy analysis reveal that their stellar populations are young and coeval, being born within the last few tens of Myr. Furthermore, because all the outlying HII regions have an estimated age of less than 30 Myr, which is at least a factor

¹⁷ We emphasize that the condition for the ram-pressure stripping is satisfied by using the relative velocity between the two galaxies along the line of sight. Possible motions in the plane of the sky would make ram pressure even more efficient.

of ten lower than the ablation time, we conclude that these star-forming regions were born in situ after the removal of gas. This point is strengthened by the observed agreement between the oxygen abundance derived spectroscopically for the HII regions ($12 + \log(O/H) = 8.38$ for C2 and $12 + \log(O/H) = 8.29$ for C6) with the one for VCC1249 obtained using the mass-metallicity relation ($12 + \log(O/H) = 8.35$).

The presence of a metal-enriched gas tail that extends to more than 3 arcmin far from VCC1249 in the direction of M49 is remarkable also in the context of the metal enrichment of low-density gas. Indeed, within dense environments such as rich clusters, ram-pressure stripping may be an effective way to transport dust and metals from the ISM of galaxies to the outer intracluster medium (Boselli & Gavazzi 2006; Cortese et al. 2010). Moreover, the encounter of VCC1249 with the halo of M49 may be the prototype of the interaction between satellite galaxies and their centrals and thus this mechanism may be responsible for at least part of the metal enrichment seen in the halos of galaxies at all redshifts (Tumlinson et al. 2011). This example shows that galactic winds may not be the only processes needed to transport metals to large galactocentric distances.

6.1. Witnessing a peculiar interaction

Witnessing this type of interaction in a cluster must be considered fortuitous, a fortiori in the nearby Virgo cluster. Considering the morphological types, systems like the VCC1249/M49 pair (a giant elliptical galaxy interacting with a dwarf irregular) are rare in nearby clusters. In fact, giant elliptical (and cD) galaxies inhabit the center of clusters, while dwarf irregular galaxies tend to populate the cluster's outskirts. The majority of dwarf galaxies suffer from one or more ram-pressure stripping events as they enter the cluster (Bekki 2009), leading to a complete removal of the atomic gas and to a consequent transformation into dwarf-ellipticals on very short time scales (Boselli et al. 2008a). Thus, because of a combined effect of a lower velocity dispersion and gas density within the cluster, systems like VCC1249/M49 would be much more frequent at higher redshift, where the population of gas-rich dwarf galaxies has not yet been quenched by ram pressure.

However, looking at low redshift, some similarities with the studied system can be found in the famous interacting pair between the giant elliptical galaxy (M86) and a giant late-type galaxy (NGC 4438) in the Virgo cluster. The highly disturbed morphology of NGC 4438 is traditionally (e.g. Boselli et al. 2005) interpreted as caused by tidal interaction with its companion galaxy NGC 4435. Kenney et al. (2008), who discovered an extended complex of H α filaments connecting NGC 4438 with M86, instead invoked ram-pressure stripping and tidal (collision) interaction with M86. The ram pressure, resulting from the passage through the halo of M86, causes the removal of most of the ISM from the stellar disk of NGC 4438, while tidal interaction produces most morphology disturbances in NGC 4438. As for VCC1249, NGC 4438 is very HI-deficient and what is believed to be the remnant of its atomic gas is observed near M86 (Li & van Gorkom 2001). Both M86 and M49 have in their proximity an unusual cloud of HI, left-over of galaxies that passed through their halos. However, nothing like the spectacular complex of H α filaments connecting NGC 4438 to M86, heated by thermal conductivity from the ICM and by turbulent shocks, is present between VCC1249 and M49, where compact H α emission is detected associated with star formation activity taking place in compact HII regions. Thus, the presence of an HI cloud displaced in the halo of an elliptical galaxy, also combined with

features visible in the UV-band and H α , could be the signature of a rich-gas galaxy crossing.

6.2. The complex diffuse structures around M49

Additional information about the dynamical history of VCC1249 may be gleaned from the tidal debris in the surrounding field. Early imaging by Patterson & Thuan (1992) and McNamara et al (1994) revealed a debris trail $\sim 2'$ in length extending northwest from VCC1249, as well as a short countertail to the southwest. More recently, Janowiecki et al (2010) used deep imaging to reveal a complex series of accretion structures around M49, some possibly associated with VCC1249. With the deep NGVS imaging presented here, and the well-determined photometric model for M49, we can now search even deeper to trace these tidal features further in extent, and search for others.

To increase signal-to-noise at faint surface brightness and highlight any diffuse structures found around M49 and VCC1249, we started with our image of the field after subtracting the best-fit elliptical isophotal model of M49 (shown in Figure 16). We then ran IRAF's OBJMASKS task to identify and mask features that are 10σ above a locally defined background measured on $1'$ scales. This effectively masks bright stars, the high surface brightness regions of M49's companion galaxies, and a myriad of fainter discrete sources on the image. We then spatially re-binned the image in 39×39 ($7.25'' \times 7.25''$) pixel bins, calculating the median pixel intensity of each bin. The combination of masking and medianing effectively rejects the contributions from small discrete sources and maps the structure of diffuse light on ~ 0.5 kpc scales.

Figure 15 shows this binned, median-smoothed map. The vertical and horizontal banding in the image are artifacts tracing the edges of the CCDs on the Megacam array. In addition to these artifacts, several diffuse features can be seen in the image. First, we trace a halo of diffuse light around VCC1249 out to a major axis radius of $\sim 2.4'$ (11 kpc). Beyond this radius, we see a stream of light extending from VCC1249 to the northwest, toward the center of M49, coincident with the extended HI and UV light. Around M49 itself, there are a number of diffuse features; of particular interest are the shells 5–10' to the northwest of M49, originally identified by Janowiecki et al (2010); their “inner shell” feature) using deep Schmidt imaging. Because the higher spatial resolution of Megacam allows better rejection of background contaminants, these shells are more clearly revealed in Figure 15, where they are resolved into two features. The innermost feature extending NW from the center of M49 shows a folded fan-like shape, very reminiscent of features that arise from radial accretion events (e.g., Hernquist & Quinn 1988). A second shell can be seen at slightly larger radius to the west-northwest of M49. Other features can be seen in the image as well, including more extended shells farther to the northwest and to the southeast, and a fan of material extending west-southwest of the center of M49. Although the connection between these very extended NW and SE shells and VCC1249 is not clear (as Janowiecki et al. 2010 have already pointed out), the better resolution of our NGVS data shows much more detail in the “inner shell”, and clearly links that feature to VCC1249. All these features are visible as well in the Schmidt imaging detailed in Janowiecki et al (2010); the fact that they are visible in both imaging surveys demonstrates that they are not simply artifacts generated by instrumental effects such as reflections or scattered light.

We focus here only on the tidal features related to VCC1249 itself. In this context, the folded fan-shaped plume to the north-

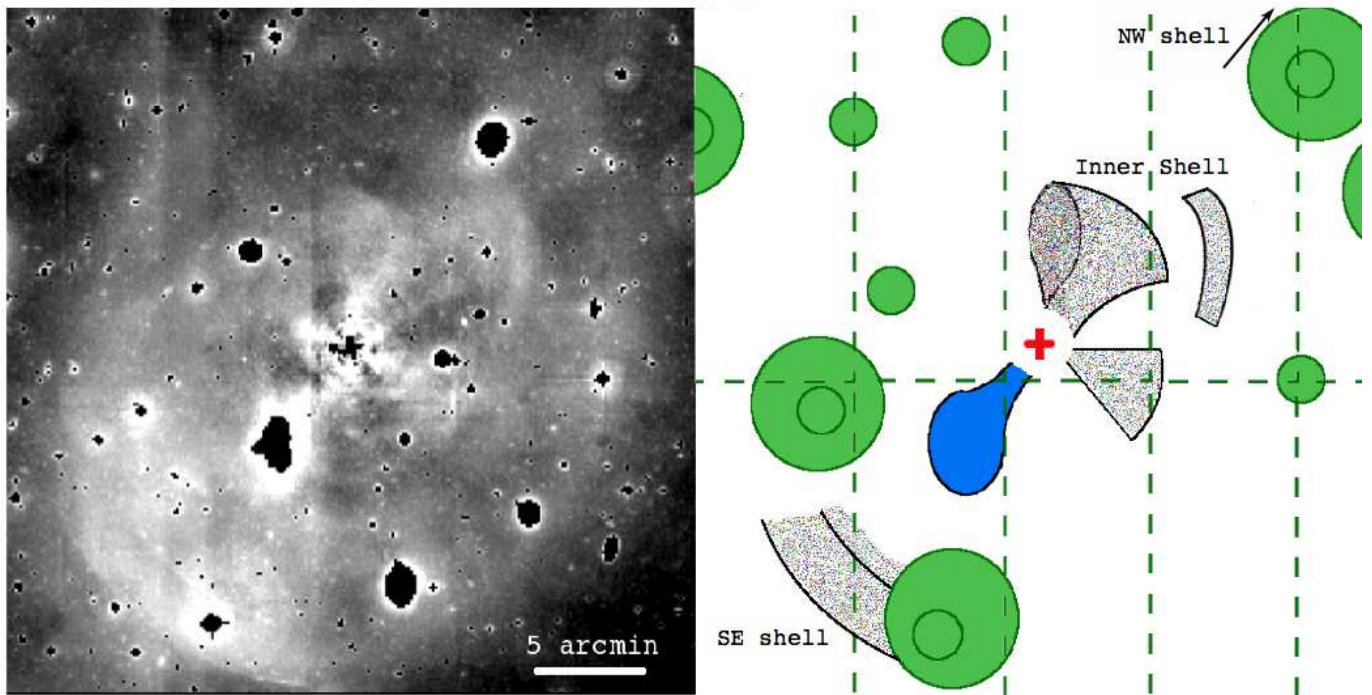


Fig. 15. Left: binned, median-smoothed grayscale map of M49 showing residuals from the ELLIPSE model in the NGVS g -band imaging. Although there are artifacts due to the edges of the CCDs and to the bright stars (circular reflection with two sizes: 1 and 3 arcmin in radius), an extensive series of shells and filaments is apparent in agreement with Janowiecki et al. (2010). Right: toy-picture highlighting the diffuse features found in the left-image: the artifacts (green), shells and fan of material described in the text (gray) and VCC1249 with its tail pointing toward M49 (blue).

west of M49 is particularly intriguing. This type of structure forms from the radial accretion of the diskly companion, as detailed in Hernquist & Quinn (1988). Indeed, a comparison between the structure seen in Figure 15 and the “ $t=225$ ” snapshot of the HQ88 disk accretion model (their Figure 2) is striking. In this scenario, VCC1249 has made (at least) two close passages past M49 with the radius of the inner NW shell showing the apocentric turning point from the previous passage. This shell occurs at a projected radius of $6.4'$ or 30 kpc from M49’s center. At this radius, the M49 mass model of Côté et al. (2003) has an enclosed mass of $2 \times 10^{12} M_{\odot}$, yielding a dynamical time of ~ 100 Myr. Since VCC1249 is currently found projected $5.6'$ (26 kpc) southeast of M49, this is also a rough lower limit on the time since the last closest passage to M49. Of course, this limit assumes that VCC1249’s orbit lies along the plane of the sky and the projected separations are true separations, which is likely not true. The fact that M49 and VCC1249 have a velocity difference of 611 km s^{-1} argues that much of the orbital motion is along the line of sight, which significantly increases the inferred time since last passage. Given these uncertainties, a scenario where VCC1249 is on a fairly radial, bound orbit with last pericenter passage occurring a few hundred Myr ago is quite reasonable; this orbital timescale is quite similar to the star formation truncation time we derived earlier (see Section 5.1) and argues for a common origin¹⁸. In this scenario, tidal stripping of material from VCC1249 is ongoing, as is ram-pressure stripping. Indeed, because according to this scenario the dwarf galaxy is on its second passage through the dense halo of M49, it likely lost a significant amount of gas on the first passage as well. This first pas-

sage could have stripped the outer, low-density gas in VCC1249, leaving the denser gas in the inner regions to be stripped on this subsequent passage we observe now.

6.3. Formation of compact objects

In addition to the interest for studies of galaxy interactions in rich clusters, isolated HII regions born from ram-pressure stripped gas provide some insight into the formation of evolved compact systems such as globular clusters (GC) and ultra compact dwarf galaxies (UCD). Found preferentially in the neighbors of massive elliptical galaxies (Hilker 2011), the origin of the latter compact systems is still controversial. Models indicate that they can form either by tidal stripping of the diffuse, low surface brightness disks of nucleated dwarf ellipticals (Bekki et al. 2003), or might derive from the merging of many young, massive ($10^6 M_{\odot}$) star clusters, born during a past merger event (Kroupa 1998; Fellhauer & Kroupa 2002; Kissler-Patig et al. 2006). The HII regions formed during the interaction of the (originally) star-forming VCC1249 with M49 might be the progenitors of these compact systems. They have very compact morphologies and are composed of coeval stars formed during a single episode of star formation. The stripped gas that gave birth to these HII regions is now (dynamically) dissociated from them and thus it cannot sustain any more star formation. Given their mass ($\sim 10^4 M_{\odot}$) and their young age (≈ 5 -10 Myr), it is still unclear whether they will survive the “infant mortality” caused by the kinetic energy injected by supernova explosions (Lada & Lada 2003). Recent models seem to indicate that at least a fraction of them should resist and end up in compact evolved systems (Gieles & Bastien 2008). Containing only $10^4 M_{\odot}$, the HII regions found around M49 certainly do not have the necessary mass to form UCDs

¹⁸ The timescale since the first passage is much longer than the derived truncation time. However, the SED analysis can only detect the last truncation event, the second passage.

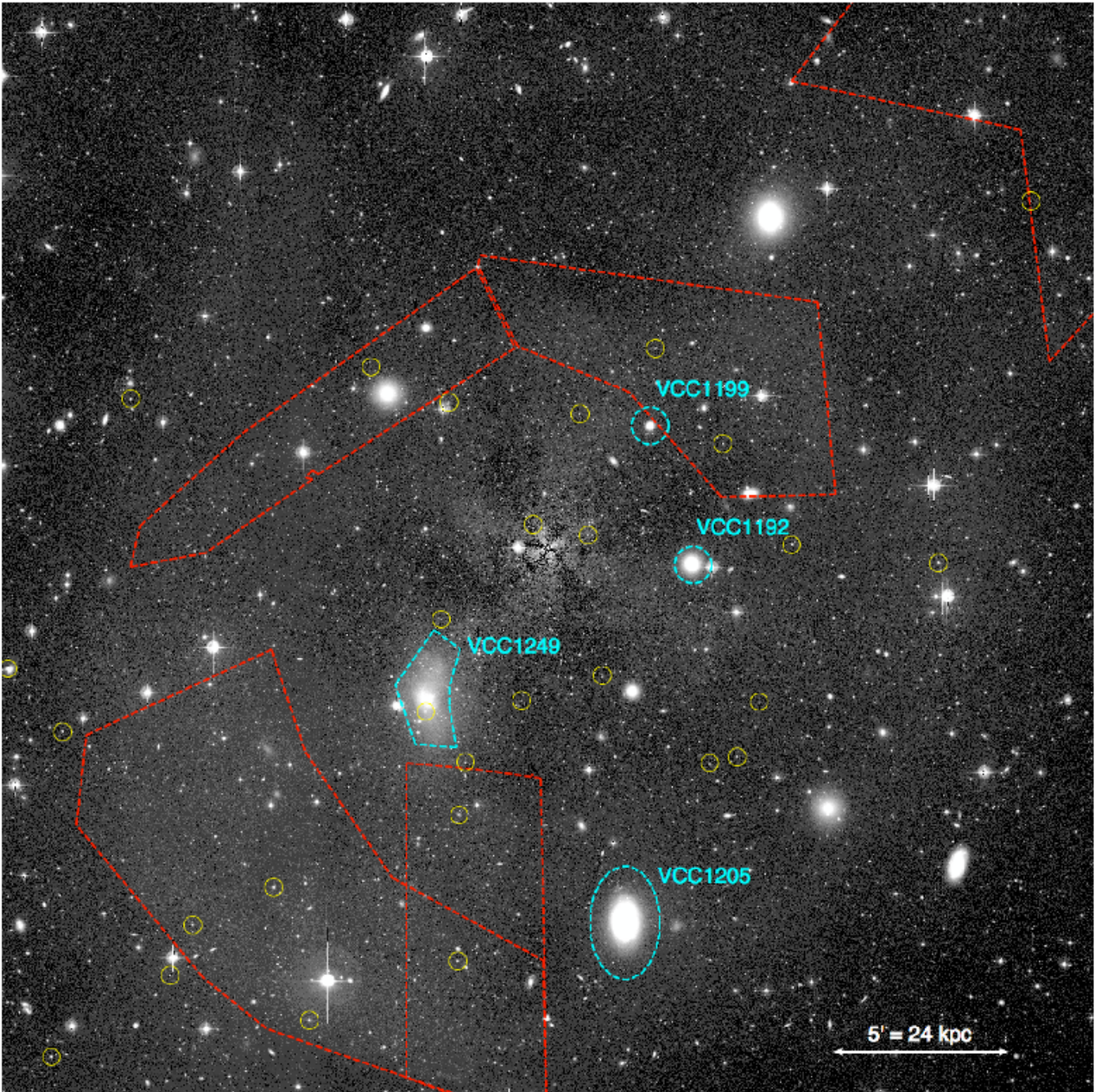


Fig. 16. Grayscale image of M49 showing residuals from the ELLIPSE model that best fits the azimuthally averaged isophotes in the NGVS g -band imaging (see Ferrarese et al. 2011). An extensive series of shells and filaments is apparent. A complex structural was also found by Janowiecki et al. (2010); the dashed red lines indicate the regions where these authors found shells and plumes in their residual image (here shown for comparison with those in Figure 15). VCC1249 is labeled in cyan, as are VCC1199 and VCC1192, two compact elliptical galaxies that have likely undergone tidal stripping (e.g., Cote et al. 2010). VCC1205 shows evidence for star formation detached from the main body of the galaxy, in the direction of M49. Yellow circles show the position of candidate UCDs (having $g \leq 21$ and effective radii in the range $10 \leq R_e \leq 100$ pc) identified from the NGVS imaging. At least some of these objects may have formed through tidal “threshing” of nucleated dwarf galaxies (e.g., Bekki et al. 2001).

or massive GCs, but only intermediate-mass compact objects. Considering however that at high redshift late-type galaxies had gas masses significantly higher than those observed in the local universe (e.g. Boselli et al. 2001), the HII regions formed during the interaction of VCC1249 with M49 could be the scaled-down version at $z = 0$ of more massive star clusters formed at

higher redshift that later transformed into today massive GCs and UCDs. Similar star-forming compact structures, but of significantly higher mass, have been indeed observed in the tails of some massive spirals in the clusters A1689 and A2667 at $z \approx 0.2$ by Cortese et al. (2007).

6.4. Conclusion

In conclusion, the interaction between VCC1249 and M49 underscores the fundamental role played by environment in shaping the properties of galaxies in cluster cores. In this particular case, VCC1249 is undergoing both ram pressure and tidal interaction: the joint action of the two mechanisms leads to the removal of the HI gas, while the morphology disturbances are triggered by the gravitational tides. Our analysis suggests that the star formation in VCC1249 was truncated 200 Myr ago, which is consistent with the gas ablation time. The HII regions were born *in situ*, within the turbulent, pre-enriched gas that was removed by the interaction.

6.5. A harsh environment: the Virgo B subcluster

We conclude with a panoramic view of the immediate neighborhood of VCC1249 — an environment that is, of course, dominated by M49, the brightest member of the Virgo cluster and the central galaxy in Virgo’s B subcluster (e.g., Binggeli, Popescu & Tammann 1993). Our analysis of VCC1249 adds to the growing body of evidence that interactions, mergers and stripping have had a profound affect on the galaxy population in this high-density environment. Figure 16 illustrates some of this evidence. In addition to VCC1249, this region also contains two examples of the rare class of “compact elliptical” galaxies, whose origin is almost certainly related to strong tidal stripping of initially more massive galaxies (e.g., Faber 1973; Bekki et al. 2001b; Chilingarian et al. 2009; Côté 2010; Huxor et al. 2011). Furthermore, as shown in the residual image in Figures 15 and 16, a complex series of shells, plumes and streams surrounds M49 — *prima facie* evidence for past accretions and interactions (Janiowiecki et al. 2010; Ferrarese et al. 2011). Fitting of PSF-convolved models to sources in the NGVS images also reveals a large number of UCDs candidates, which are shown as the yellow circles in Figure 16 (see also Håşegan et al. 2005). Although there may well be multiple formation channels for UCDs, at least some of these objects could have formed through tidal “threshing” of nucleated dwarf galaxies, a leading UCD formation mechanism (Bekki et al. 2001a). Finally, approximately 11’ to the south of M49 lies VCC1205, which is classified as ScIII-pec by Binggeli et al. (1985). Despite its high relative velocity with respect to M49 ($\Delta v = v_{M49} - v_{VCC1205} = 1001 - 2341 = 1340 \text{ km s}^{-1}$), the galaxy shows a minor HI deficiency, while its optical and NUV morphology shows evidence for star-forming regions detached from the main body of the galaxy in the direction of M49 (Figure 17). This is perhaps another indication of the harsh environment existing in the core of the Virgo subcluster B. In any case, there is mounting evidence that the central regions of rich clusters — and of the Virgo B subcluster in particular — are highly dynamic environments in which interactions influence the structure of both the central galaxies and their surrounding satellites.

7. Acknowledgments

We warmly thank Mattia Fumagalli for his precious contribution on the SED fitting procedures. We really appreciated the help provided by J. Xavier Prochaska in obtaining Keck data. This work made extensive use of GoldMine, the Galaxy On Line Database (<http://goldmine.mib.infn.it>). We are grateful to P. Franzetti and M. Hilker for constructive discussions. We thank Joseph F. Hennawi for his useful comments on the draft. Some of the data presented herein were obtained at the

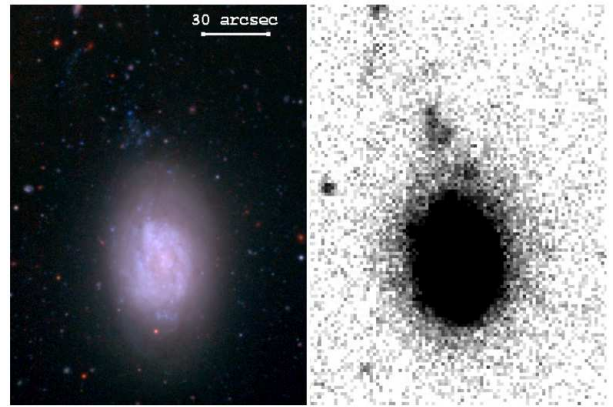


Fig. 17. Left: RGB image of VCC1205 obtained by combining the NGVS images in the u, g, z filters. Right: NUV image of VCC1205 on the same scale. Blue extended star-forming regions are visible in the north direction (toward M49).

W.M. Keck Observatory, which is operated as a scientific partnership among the California Institute of Technology, the University of California and the National Aeronautics and Space Administration. The Observatory was made possible by the generous financial support of the W.M. Keck Foundation. The authors wish to recognize and acknowledge the very significant cultural role and reverence that the summit of Mauna Kea has always had within the indigenous Hawaiian community. We are most fortunate to have the opportunity to conduct observations from this mountain. The present study could not have been conceived without the DR7 of SDSS. Funding for the Sloan Digital Sky Survey (SDSS) and SDSS-II has been provided by the Alfred P. Sloan Foundation, the Participating Institutions, the National Science Foundation, the U.S. Department of Energy, the National Aeronautics and Space Administration, the Japanese Monbukagakusho, and the Max Planck Society, and the Higher Education Funding Council for England. The SDSS Web site is <http://www.sdss.org/>. The SDSS is managed by the Astrophysical Research Consortium (ARC) for the Participating Institutions. The Participating Institutions are the American Museum of Natural History, Astrophysical Institute Potsdam, University of Basel, University of Cambridge, Case Western Reserve University, The University of Chicago, Drexel University, Fermilab, the Institute for Advanced Study, the Japan Participation Group, The Johns Hopkins University, the Joint Institute for Nuclear Astrophysics, the Kavli Institute for Particle Astrophysics and Cosmology, the Korean Scientist Group, the Chinese Academy of Sciences (LAMOST), Los Alamos National Laboratory, the Max-Planck-Institute for Astronomy (MPIA), the Max-Planck-Institute for Astrophysics (MPA), New Mexico State University, Ohio State University, University of Pittsburgh, University of Portsmouth, Princeton University, the United States Naval Observatory, and the University of Washington.

GALEX is a NASA Small Explorer, launched in 2003 April. We gratefully acknowledge NASA’s support for construction, operation and science analysis for the GALEX mission, developed in cooperation with the Centre National d’Etudes Spatiales (CNES) of France and the Korean Ministry of Science and Technology. The research leading to these results has received funding from the European Community’s Seventh Framework Programme (/FP7/2007-2013/) under grant agreement No 229517.

This work is supported in part by the Canadian Advanced

Network for Astronomical Research (CANFAR) which has been made possible by funding from CANARIE under the Network-Enabled Platforms program.

G. Gavazzi acknowledges financial support from Italian MIUR PRIN contract 200854ECE5 and from the high energy contract ASI-INAF I/009/10/0. J.C. Mihos thanks the National Science Foundation for support through awards ASTR-0607526 and AST-0707793.

We thank the Referee for the thorough reading of the manuscript and helpful comments.

References

- Althaus, L. G., & Benvenuto, O. G. 1997, *ApJ*, 477, 313
- Asplund, M., Grevesse, N., Sauval, A. J., & Scott, P. 2009, *ARA&A*, 47, 481
- Binggeli, J. A., Phillips, M. M., & Terlevich, R. 1981, *PASP*, 93, 5
- Bekki, K., Couch, W. J., & Drinkwater, M. J. 2001, *ApJ*, 552, L105
- Bekki, K., Couch, W. J., Drinkwater, M. J., & Gregg, M. D. 2001, *ApJ*, 557, L39
- Bekki, K., Couch, W. J., Drinkwater, M. J., & Shioya, Y. 2003, *MNRAS*, 344, 399
- Bekki, K. 2009, *MNRAS*, 399, 2221
- Bessell, M. S. 2001, *PASP*, 113, 66
- Binggeli, B., Sandage, A., & Tammann, G. A. 1985, *AJ*, 90, 1681
- Binggeli, B., Popescu, C. C., & Tammann, G. A. 1993, *A&AS*, 98, 275
- Blakeslee, J. P., Jordán, A., Mei, S., et al. 2009, *ApJ*, 694, 556
- Boselli, A., Gavazzi, G., Donas, J., Scodreggio, M. 2001, *AJ*, 121, 753
- Boselli, A., & Gavazzi, G. 2002, *A&A*, 386, 124
- Boselli, A., Boissier, S., Cortese, L., et al. 2005, *ApJ*, 623, L13
- Boselli, A., & Gavazzi, G. 2006, *PASP*, 118, 517
- Boselli, A., Boissier, S., Cortese, L., & Gavazzi, G. 2008a, *ApJ*, 674, 742
- Boselli, A., Boissier, S., Cortese, L., & Gavazzi, G. 2008b, *A&A*, 489, 1015
- Boselli, A., Boissier, S., Heinis, S., et al. 2011, *A&A*, 528, L4107
- Chilingarian, I., Cayatte, V., Revaz, Y., et al. 2009, *Science*, 326, 1379
- Côté, P., McLaughlin, D. E., Cohen, J. G., & Blakeslee, J. P. 2003, *ApJ*, 591, 850
- Côté, P. 2010, *American Institute of Physics Conference Series*, 1240, 331
- Chung, A., van Gorkom, J. H., Kenney, J. D. P., & Vollmer, B. 2007, *ApJ*, 659, L115
- Chung, A., van Gorkom, J. H., Kenney, J. D. P., Crowl, H., & Vollmer, B. 2009, *AJ*, 138, 1741
- Cortese, L., Hughes, T. 2009, *MNRAS*, 400, 1225
- Cortese, L., Gavazzi, G., Boselli, A., et al. 2006, *A&A*, 453, 847
- Cortese, L., Marcellac, D., Richard, J., et al. 2007, *MNRAS*, 376, 157
- Cortese, L., Boselli, A., Franzetti, P., et al. 2008, *MNRAS*, 386, 1157
- Cortese, L., Davies, J., Pohlen, M., et al. 2010, *A&A*, 518, L49
- Denicoló, G., Terlevich, R., & Terlevich, E. 2002, *MNRAS*, 330, 69
- Domainko, W., et al. 2006, *A&A*, 452, 795
- Dopita, M. A., & Evans, I. N. 1986, *ApJ*, 307, 431
- Dressler, A., Smail, I., Poggianti, B. M., et al. 1999, *ApJS*, 122, 51
- Drinkwater, M. J., Jones, J. B., Gregg, M. D., & Phillipps, S. 2000, *PASA*, 17, 227
- Duc, P.-A., & Renaud, F. 2011, *arXiv:1112.1922*
- Dutil, Y., & Roy, J.-R. 1999, *ApJ*, 516, 62
- Faber, S. M. 1973, *ApJ*, 179, 423
- Fabian, A. C., 1985, in *New Aspect of Galaxy Photometry*, ed. J.-L. Nieto (Berlin: Springer-Verlag), p. 95.
- Fellhauer, M., & Kroupa, P. 2002, *MNRAS*, 330, 642
- Ferrarese, L., Côté, P., Jordán, A., et al. 2006, *ApJS*, 164, 334
- Ferrarese et al. 2011, *ApJS*, submitted
- Fioc, M., & Rocca-Volmerange, B. 1997, *A&A*, 326, 950
- Forman, W., Jones, C., & Tucker, W. 1985, *ApJ*, 293, 102
- Franzetti, P., Scodreggio, M., Garilli, B., Fumana, M., & Paioro, L. 2008, *Astronomical Data Analysis Software and Systems XVII*, 394, 642
- Fumagalli, M., Gavazzi, G., Scaramella, R., & Franzetti, P. 2011, *A&A*, 528, A46
- Gavazzi, G., Boselli, A., Scodreggio, M., Pierini, D., & Belsole, E. 1999, *MNRAS*, 304, 595
- Gavazzi, G., Boselli, A., Mayer, L., et al. 2001, *ApJ*, 563, L23
- Gavazzi, G., Bonfanti, C., Sanvito, G., Boselli, A., & Scodreggio, M. 2002, *ApJ*, 576, 135
- Gavazzi, G., Boselli, A., Donati, A., Franzetti, P., & Scodreggio, M. 2003, *A&A*, 400, 451
- Gavazzi, G., Zaccardo, A., Sanvito, G., Boselli, A., & Bonfanti, C. 2004, *A&A*, 417, 499
- Gavazzi, G., Fumagalli, M., Cucciati, O., & Boselli, A. 2010, *arXiv:1003.3795*
- Geisler, D. 1996, *AJ*, 111, 480
- Gieles, M., Bastian, N., 2008, *A&A*, 482, 165
- Groenewegen, M. A. T., & de Jong, T. 1993, *A&A*, 267, 410
- Gunn, J. E., & Gott, J. R., III 1972, *ApJ*, 176, 1
- Haşegan, M., Jordán, A., Côté, P., et al. 2005, *ApJ*, 627, 203
- Haynes, M. P., & Giovanelli, R. 1984, *AJ*, 89, 758
- Haynes, M. P., Giovanelli, R., Salzer, J. J., et al. 1999, *AJ*, 117, 1668
- Henning, P. A., Sancisi, R., & McNamara, B. R. 1993, *A&A*, 268, 536
- Hernquist, L., & Quinn, P. J. 1988, *ApJ*, 331, 682
- Hester, J. A., et al. 2010, *ApJ*, 716, L14
- Hoffman, G. L., Glossov, J., Helou, G., Salpeter, E. E., & Sandage, A. 1987, *ApJS*, 63, 247
- Huchra, J. 1985, private communication cited in Sancisi et al. (1987)
- Huxor, A. P., Phillipps, S., Price, J., & Harniman, R. 2011, *MNRAS*, 414, 3557
- Idiart, T. P., Silk, J., & de Freitas Pacheco, J. A. 2007, *MNRAS*, 381, 1711
- Izotov, Y. I., Stasińska, G., Meynet, G., Guseva, N. G., & Thuan, T. X. 2005, *VizieR Online Data Catalog*, 3448, 80955
- Janowiecki, S., Mihos, J. C., Harding, P., et al. 2010, *ApJ*, 715, 972
- Kapferer, W., Sluka, C., Schindler, S., Ferrari, C., & Ziegler, B. 2009, *A&A*, 499, 87
- Kenney, J. D. P., & Koopmann, R. A. 1999, *AJ*, 117, 181
- Kenney, J. D. P., Tal, T., Crowl, H. H., Feldmeier, J., & Jacoby, G. H. 2008, *ApJ*, 687, L69
- Kennicutt, R. C., Jr., Edgar, B. K., & Hodge, P. W. 1989, *ApJ*, 337, 761
- Kennicutt, R. C., Jr. 1998, *ApJ*, 498, 541
- Kewley, L. J., & Dopita, M. A. 2002, *ApJS*, 142, 35
- Kewley, L. J., & Ellison, S. L. 2008, *ApJ*, 681, 1183
- Kissler-Patig, M., Jordán, A., & Bastian, N. 2006, *A&A*, 448, 1031
- Kobulnicky, H. A., & Kewley, L. J. 2004, *ApJ*, 617, 240
- Krishna Kumar, C., & Thonnard, N. 1983, *AJ*, 88, 260
- Kroupa, P. 1998, *MNRAS*, 300, 200
- Lada, C., Lada, E., 2003, *ARA&A*, 41, 57
- Lee, M. G., Kim, E., & Geisler, D. 1997, *AJ*, 114, 1824
- Lee, H., Richer, M. G., & McCall, M. L. 2000, *ApJ*, 530, L17
- Lee, H., McCall, M. L., & Richer, M. G. 2003, *AJ*, 125, 2975
- Lee, J. C., Gil de Paz, A., Tremonti, C., et al. 2009, *ApJ*, 706, 599
- Li, Y., & van Gorkom, J. H. 2001, *Gas and Galaxy Evolution*, 240, 637
- Mayer, L., Mastrogiro, C., Wadsley, J., Stadel, J., & Moore, B. 2006, *MNRAS*, 369, 1021
- McGaugh, S. S. 1991, *ApJ*, 380, 140
- McNamara, B. R., Sancisi, R., Henning, P. A., & Junor, W. 1994, *AJ*, 108, 844
- Mei, S., Blakeslee, J. P., Côté, P., et al. 2007, *ApJ*, 655, 144
- Mieske, S., Hilker, M., Jordán, A., et al. 2008, *A&A*, 487, 921
- Nilson, P. 1973, *Nova Acta Regiae Soc. Sci. Upsaliensis Ser. V*, 0
- Oke, J. B., Cohen, J. G., Carr, M., et al. 1995, *PASP*, 107, 375
- Oosterloo, T., & Shostak, G. S. 1984, private communication cited in Sancisi et al. (1987)
- Osterbrock, D. E. 1989, Research supported by the University of California, John Simon Guggenheim Memorial Foundation, University of Minnesota, et al. Mill Valley, CA, University Science Books, 1989, 422 p.,
- Patterson, R. J., & Thuan, T. X. 1992, *ApJ*, 400, L55
- Patterson, R. J., & Thuan, T. X. 1996, *ApJS*, 107, 103
- Pettini, M., & Pagel, B. E. J. 2004, *MNRAS*, 348, L59
- Poggianti, B. M., Bridges, T. J., Komiyama, Y., et al. 2004, *ApJ*, 601, 197
- Sancisi, R., Thonnard, N., & Ekers, R. D. 1987, *ApJ*, 315, L39
- Sandage, A. 1986, *A&A*, 161, 89
- Schechter, P. L. 1980, *AJ*, 85, 801
- Schlegel, D. J., Finkbeiner, D. P., & Davis, M. 1998, *ApJ*, 500, 525
- Sivanandam, S., Rieke, M. J., & Rieke, G. H. 2010, *ApJ*, 717, 147
- Smith, R. J., Lucey, J. R., Hammer, D., et al. 2010, *MNRAS*, 408, 1417
- Sun, M., Donahue, M., Roediger, E., et al. 2010, *ApJ*, 708, 946
- Thomas, D., Maraston, C., Bender, R., & Mendes de Oliveira, C. 2005, *ApJ*, 621, 673
- Tumlinson, J., Thom, C., Werk, J. K., et al. 2011, *Science*, 334, 948
- Vollmer, B. 2003, *A&A*, 398, 525
- Vollmer, B., Huchtmeier, W., & van Driel, W. 2005, *A&A*, 439, 921
- Woolley, S. E., & Weaver, T. A. 1995, *ApJS*, 101, 181
- Yagi, M., Yoshida, M., Komiyama, Y., et al. 2010, *AJ*, 140, 1814
- Zaritsky, D., Kennicutt, R. C., Jr., & Huchra, J. P. 1994, *ApJ*, 420, 87